CHAPTER III
ANION EXCHANGE AND CATALYTIC PROPERTIES OF A SERIES OF Zn(II)-4,4'-BPY-CARBOXYLATO FRAMEWORKS

3.1 Introduction

Porous coordination polymers (PCPs) may find potential applications in molecular adsorption and separation processes,[1,74] ion-exchange,[60] catalysis,[41-55] sensor technology,[75] and optoelectronics.[76] The design of porous coordination polymers does not only allow the preparation of light materials with high porosity, but also the generation of desirable regular networks. Despite extensive studies, applications of porous compounds are still quite limited compared to that of zeolites. Inorganic materials with inner cavities, such as zeolites are known to bind many organic molecules in the hollow spaces and often exhibit unique catalytic properties for a number of organic reactions, in which high regioselectivity, stereoselectivity, and shape selectivity are observed.[76] Reports of catalytic studies involving coordination polymers have been relatively scarce.[41-55] While most of these investigations have dealt with some significant successes in enantioselective catalysis, there has been little focus thus far on probing the selectivity with substrates of comparable size to the pore dimensions.

Recently, the anion exchange behavior of some coordination polymers has been examined and the results highlighted the potential applications of the polymers to anion sequestering[77] and sensing.[78] The anion-exchange and catalytic applications of monocarboxylato-bridged porous coordination polymers have been rarely reported.[78] On the basis of these studies, the structures of three porous coordination polymers, *i.e.* the three-dimensional framework, $\{[Zn_3(\mathbf{4,4'\text{-}bpy})_{3.5}(\mu\text{-}OOCH)_4(H_2O)_2](ClO_4)_2(H_2O)_2\}_n$ (**1**), the one-dimensional three-leg ladder $\{[Zn_3(\mathbf{4,4'\text{-}bpy})_3(\mu\text{-}OOCCH_3)_4(H_2O)_2](PF_6)_2(H_2O)_2\}_n$ (**6**), and the two-dimensional layered network $\{[Zn_3(\mathbf{4,4'\text{-}bpy})_4(\mu\text{-}OOCCH_2CH_3)_4](ClO_4)_2(\mathbf{4,4'\text{-}bpy})_2(H_2O)_4\}_n$ (**7**) are describes and compared with those of the remaining compounds (**2-5** and **8-11**). The structural data of these compounds are given in supplementary data except $\{[Zn_3(\mathbf{4,4'\text{-}bpy})_{3.5}(\mu\text{-}OOCH)_4$

$(H_2O)_2](BF_4)_2(H_2O)_2\}_n$ (**3**) since the crystals of this compound appeared not good enough for X-ray structure analysis, thus the structure of this compound has been proposed by elemental microanalyses and spectroscopic properties. The thermal and optical properties, potential cation-exchange properties with structure retention by doping zinc(II) compounds with copper(II) and manganese(II), dynamic structural transformation by removal and reintroduction of guest molecules, anion-exchange and catalytic reactivity of all frameworks in a series of zinc(II)-**4,4'-bpy**-carboxylato compounds are investigated.

3.2 Crystal structures of $\{[Zn_3(4,4'\text{-bpy})_{3.5}(\mu\text{-}O_2CH)_4(H_2O)_2](ClO_4)_2(H_2O)_2\}_n$ (1), $\{[Zn_3(4,4'\text{-bpy})_3(\mu\text{-}O_2CCH_3)_4(H_2O)_2](PF_6)_2(H_2O)_2\}_n$ (6) $\{[Zn_3(4,4'\text{-bpy})_4(\mu\text{-}O_2CCH_2CH_3)_4](4,4'\text{-bpy})_2(ClO_4)_2(H_2O)_4\}_n$ (7)

3.2.1 Crystal Structure Determination

The X-ray single-crystal data for all compounds were collected at 293(2) K on a 1 K Bruker SMART CCD area detector diffractometer using graphite monochromated Mo Kα radiation (λ = 0.71073 Å) at a detector distance of 4.5 cm and swing angle of –35°. A hemisphere of the reciprocal space was covered by combination of three sets of exposures; each set had a different ϕ angle (0°, 88°, and 180°) and each exposure of 40 s covered 0.3° in ω. Data reduction and cell refinements were performed using the program SAINT.[79] An empirical absorption correction by using the SADABS[80] program was applied, which resulted in transmission coefficients ranging from 0.847 to 1.000, 0.654 to 1.000 and 0.737 to 1.000 for compounds **1**, **6** and **7**, respectively. The structures were solved by direct methods and refined by full-matrix least-squares method on $(F_{obs})^2$ with anisotropic thermal parameters for all non-hydrogen atoms using the SHELXTL-PC V 6.12 software package.[81] All hydrogen atoms were located geometrically and refined isotropically except hydrogen atoms of the propionate group in compound **7**. The molecular graphics were created by using the SHELXTL-PC[81] package. The crystal and refinement details of three compounds are listed in Table 3.1, selected bond lengths and angles are given in Tables 3.2, 3.3 and 3.4, respectively.

For compound **1**, displacement parameter restrains were used in modeling the perchlorates and the **4,4'-bpy** ligands. Even with these, the displacement parameter

ratio (max:min) of a few atoms is relatively high (4.5:1), and the anisotropic parameters for the perchlorate are larger than ideal. The crystal and refinement details of the remaining compounds (**2-5** and **8-11**) are given in supplementary data (on CD-ROM inside the back cover of this thesis).

Table 3.1 Crystal and refinement data for compounds **1**, **6** and **7**

Compound	**1**	**6**	**7**
Empirical formula	$C_{39}H_{40}Cl_2N_7O_{20}Zn_3$	$C_{38}H_{44}F_{12}N_6O_{12}P_2Zn_3$	$C_{72}H_{76}Cl_2N_{12}O_{20}Zn_3$
Formula weight	1193.86	1258.87	1696.46
T (K)	293(2)	293(2)	293(2)
Crystal system	Monoclinic	Triclinic	Monoclinic
Space group	$C2/c$	$P\bar{1}$	$P2_1/c$
a (Å)	26.8795(12)	10.6952(7)	18.506(4)
b (Å)	19.1415(8)	11.4831(7)	18.838(4)
c (Å)	21.2041(9)	11.7638(7)	25.568(5)
α (°)	90	101.558(2)	90
β (°)	122.078(2)	116.757(2)	119.90(3)
γ (°)	90	95.574(2)	90
V (Å^3)	9244.2(7)	1234.58(13)	7727(3)
Z	8	1	4
D_{cal} (g cm^{-3})	1.716	1.677	1.458
μ (mm^{-1})	1.748	1.617	1.071
F(000)	4856	630	3504
θ range (°)	2.22 -21.99	2.02-30.35	2.16 -27.48
GOF	1.03041	1.002	1.023
Final R indices	$R1$ = 0.0465	$R1$ = 0.0648	$R1$ = 0.0562
[I>2σ(I)]	$wR2$ = 0.1116	$wR2$ = 0.1666	$wR2$ = 0.1223
R indices (all data)	$R1$ = 0.0623	$R1$ = 0.0895	$R1$ = 0.0897
	$wR2$ = 0.1206	$wR2$ = 0.1867	$wR2$ = 0.1332
Largest difference peak and hole (e Å^{-3})	0.727, –0.981	1.460, –1.905	0.417, –0.564

$R = \sum||F_o| - |F_c||/\sum|F_o|$, $R_w = [\sum w\{|F_o| - |F_c|\}^2/\sum w|F_o|^2]^{1/2}$.

Table 3.2 Selected bond lengths (Å) and angles (°) for **1**

Bond lengths			
Zn1–O1	2.100(3)	Zn2–O4	2.054(5)
Zn1–O2	2.048(3)	Zn2–O5	2.062(5)
Zn1–O3	2.082(3)	Zn2–O9	2.095(3)
Zn1–O9	2.639(3)	Zn2–O9c	2.095(3)
Zn1–N1	2.168(3)	Zn2–N2a	2.198(4)
Zn1–N3	2.171(3)	Zn2–N2b	2.198(4)
Zn3–O3	2.149(3)	Zn4–O6	2.036(5)
Zn3–O3d	2.149(3)	Zn4–O7	2.065(4)
Zn3–O12	2.082(3)	Zn4–O8	2.192(3)
Zn3–O12d	2.082(3)	Zn4–O24	2.144(4)
Zn3–N5	2.126(3)	Zn4–N4f	2.150(4)
Zn3–N5d	2.126(3)	Zn4–N7	2.163(4)
Bond angles			
O1–Zn1–O3	122.98(11)	O4–Zn2–O9	97.25(9)
O3–Zn1–O2	100.69(12)	O9–Zn2–O5	82.75(9)
O2–Zn1–O9	83.07(9)	O5–Zn2–O9c	82.75(9)
O9–Zn1–O1	53.31(9)	O9c–Zn2–O4	97.25(9)
N1–Zn1–N3	175.19(15)	N2a–Zn2–N2b	180.00(15)
O3–Zn3–O12	87.99(11)	O6–Zn4–O7	114.80(18)
O12–Zn3–O3d	92.01(11)	O7–Zn4–O8	84.76(13)
O3d–Zn3–O12d	87.99(11)	O8–Zn4–O24	77.31(13)
O12d–Zn3–O3	92.01(11)	O24–Zn4–O6	83.12(18)
N5–Zn3–N5d	180.00(11)	N4f–Zn4–N7	178.21(16)

Symmetry operations: a = 1x, y, 1/2– z; b = 1–x, y, 3/2–z; c = 1–x, –y, 1–z; d = x, – y, – 1/2+z; f = 3/2–x, 1/2+y, 3/2–z

Table 3.3 Selected bond lengths (Å) and angles (°) for **6**

Bond lengths			
Zn1–O1	1.995(4)	Zn2–O2	2.076(3)
Zn1–O3	2.218(3)	Zn2–O3	2.160(3)
Zn1–O4	2.241(4)	Zn2–N3	2.177(4)
Zn1–O5	2.060(3)		
Zn1–N1	2.168(4)		
Zn1–N2a	2.211(4)		
Bond angles			
O1–Zn1–O3	104.77(13)	O2–Zn2–O3	87.73(13)
O3–Zn1–O4	58.34(12)	O3–Zn2–O2c	92.27(13)
O4–Zn1–O5	92.86(13)	N3–Zn2–N3c	180.00(12)
O5–Zn1–O1	104.03(13)		
N1–Zn1–N2a	178.29(12)		

Symmetry operations: a = x, –y+1, z; c = 1–x, 1–y, 1–z.

Table 3.4 Selected bond lengths (Å) and angles (°) for **7**

Bond lengths			
Zn1–O2	2.119(2)	Zn2–O1	2.003(2)
Zn1–O4	2.133(2)	Zn2–O3	2.166(2)
Zn1–O6a	2.083(2)	Zn2–O4	2.218(2)
Zn1–O7a	2.152(2)	Zn2–N3	2.202(3)
Zn1–N1	2.174(3)	Zn2–N5	2.198(3)
Zn1–N2	2.167(3)	Zn2–N11	2.121(3)
Zn3–O5	1.995(2)	O2–Zn1–O4	89.74(9)
Zn3–O7	2.215(2)	O4–Zn1–O6a	89.58(10)
Zn3–O8	2.168(2)	O6a–Zn1–O7a	91.47(9)
Zn3–N6	2.206(3)	O7a–Zn1–O2	89.22(9)
Zn3–N4b	2.198(3)	N1–Zn1–N2	176.37(11)
Zn3–N12c	2.108(3)		

Bond angles			
O1–Zn2–O4	105.33(9)	O5–Zn3–O7	103.28(9)
O4–Zn2–O3	59.55(9)	O7–Zn3–O8	59.57(9)
O3–Zn2–N11	95.36(10)	O8–Zn3–N12c	96.89(10)
N11–Zn2–O1	99.75(11)	N12c–Zn3–O5	100.31(11)
N3–Zn2–N5	178.24(11)	N6–Zn3–N4b	175.86(11)

Symmetry operations: a = –x, – y+1, –z; b = x– 1, y, z– 1; c = –x, –y+2, –z; d = –x+1, –y+1, –z+1.

3.2.2 Structure Description

Crystal structure of $\{[Zn_3(4,4'\text{-bpy})_{3.5}(\mu\text{-}O_2CH)_4(H_2O)_2](ClO_4)_2(H_2O)_2\}_n$ (1)

The 3D structure of compound **1** exhibits four different types of zinc(II) ions, each with octahedral N_2O_4 coordination environments (Figure 3.1). The basal plane of the octahedron around Zn1 is formed by four oxygen atoms belonging to three formato ligands. The axial positions are occupied by two pyridine N-donors from two different (bridging) **4,4'-bpy** moieties (for the atom Zn3, the **4,4'-bpy** units act as monodentate ligands; see green **4,4'-bpy** ligands in Figure 3.2). The formato ligand [O2,O12] acts as a bridging μ-O,O' ligand, connecting Zn1 to Zn3 (Figure 3.1). The formato ligand [O3,O8] functions as a μ_3-O,O,O' ligand, bridging Zn1 and Zn3 and connecting the {Zn1, O3, Zn3} unit to an adjacent Zn4 ion (through the oxygen atom O8). The third formato ligand [O1,O9] is chelating the atom Zn1 (Figure 3.1) and is coordinated as well (through the atom O9) to a neighboring Zn2 ion, thus acting as a μ-O,O',O' ligand.

Figure 3.1 Representation of the asymmetric unit of **1** showing the atom labeling scheme for the zinc(II) ions. The perchlorate anions, the lattice water molecules and the H atoms are not shown for clarity.

The Zn–O and Zn–N bond distances are in normal ranges for this type of chromophore (Table 3.2).[82] The coordination angles, varying from 53.31(9) to 122.98(11)° (Table 3.2), reflect a strong distortion of the octahedron which is principally due to the very small bite angle of the chelating formato ligand.

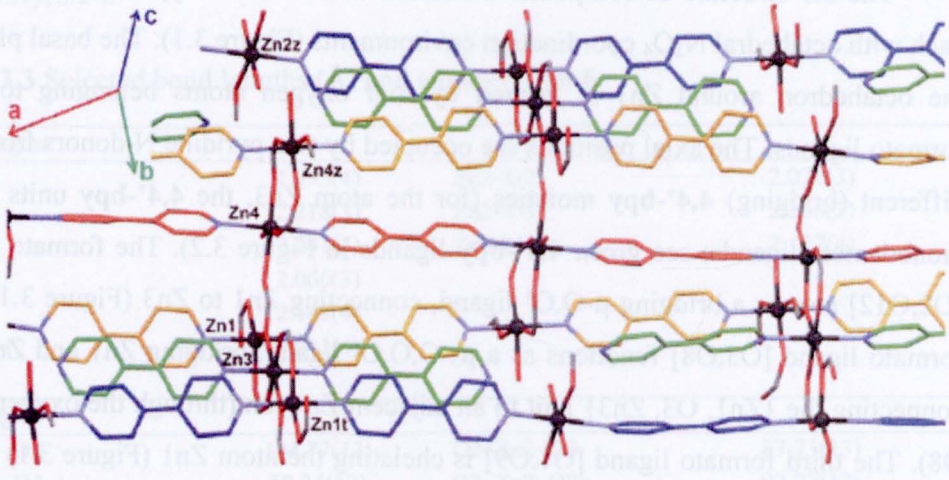

Figure 3.2 3D coordination network of Zn(II), 4,4'-bipyridine and formate. The **4,4'-bpy** ligands involved in the formation of trinuclear zinc units are shown in blue, green and orange for comparison with compounds **6** and **7**. The **4,4'-bpy** ligands generating a 1D chain are depicted in red.

The basal plane of the octahedron around Zn2 is constituted of two oxygen atoms (O9 and O9c) from two μ-O,O',O'-formato ligands and two water oxygen atoms (O4 and O5). Zn2 lies on a two-fold axis and is coordinated by two different **4,4'-bpy** moieties (N2a and N2b) at the axial positions. The Zn–O and Zn–N bond distances can be considered as normal for this type of coordination environment (Table 3.2). The basal angles ranging from 82.75(9) to 97.25(9)° indicate a distortion of the octahedral geometry, attributed to constraints induced by the bridging of the μ-O,O',O'-formato ligands to Zn1.

The N_2O_4 coordination environment around the Zn3 ion, which lies on an inversion centre, is an almost perfect octahedron (the basal angles vary from 87.99(11) to 92.01(11); Table 3.2), with four in-plane oxygen atoms belonging to distinct formato ligands (O3, O12, O3d and O12d; Figure 3.1). The axial positions are occupied by the nitrogen atoms N5 and N5d from two **4,4'-bpy** ligands. The Zn–O and Zn–N bond lengths are in common ranges.

The distorted octahedral geometry around Zn4 (the basal angles range from 77.31(13) to 114.80(18)° is most likely due to the bite angle of the μ-O,O'-formato ligands (oxygen atoms O6 and O7), connecting Zn4 to a symmetry-related Zn4 ion (see Figure 3.2). The Zn–O and Zn–N bond distances are in the normal ranges.

The self-assembly between these bridging N- and O-ligands and zinc(II) ions gives rise to a remarkable 3D architecture (Figure 3.2). The metal-organic framework is formed from trinuclear [Zn1, Zn3, Zn1] clusters which are connected through two **4,4'-bpy** ligands (yellow and blue **4,4'-bpy** ligands in Figure 3.2) to the Zn2 and Zn4 ions, generating 1D, triple-stranded infinite chains. These chains showing π–π interactions between three **4,4'-bpy** units (with centroid-to-centroid distances ranging from 3.491(4) to 3.839(4) Å) are connected to each other via a different infinite single chain exhibiting the sequence {Zn1, Zn4, Zn4, Zn1, Zn2,...} (chain built from the orange marked **4,4'-bpy** ligands in Figure 3.2). This spatial arrangement produces a unique heptanuclear coordination metallacycle (Figure 3.3).

The organization of these heptanuclear motifs in the crystal lattice gives rise to the formation of channels which are filled by disordered perchlorates and water molecules (Figure 3.4).

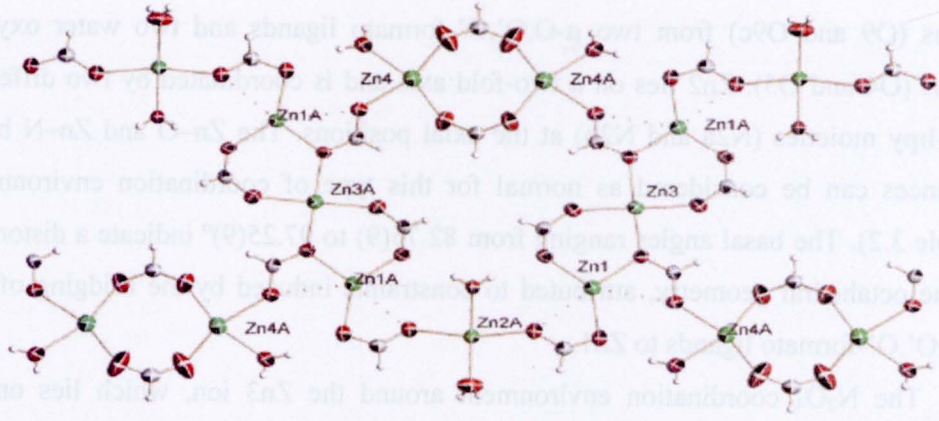

Figure 3.3 Heptanuclear building unit constituting the channel walls in **1**.

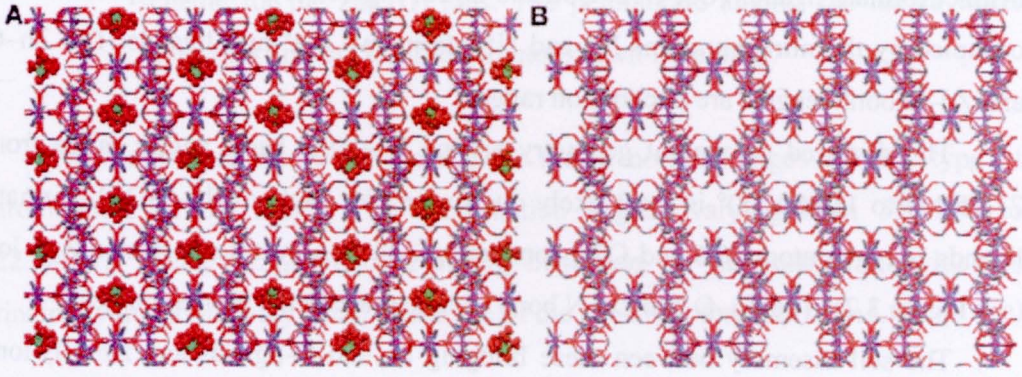

Figure 3.4 (A) Channels filled with disordered perchlorate anions (shown in the space-filling mode) and water molecules. (B) Empty channels for **1**.

Crystal structure of $\{[Zn_3(4,4'\text{-bpy})_3(\mu\text{-}O_2CCH_3)_4(H_2O)_2](PF_6)_2(H_2O)_2\}_n$ (6)

The simple replacement of formate by acetate during the synthetic procedure (used to prepare **1**) produces significant structural changes in the crystal lattice of the resulting coordination compound $\{[Zn_3(\mathbf{4,4'\text{-}bpy})_3(\mu\text{-}O_2CCH_3)_4(H_2O)_2](PF_6)_2(H_2O)_2\}_n$ (**6**). As is shown in Figure 3.5, compound **6** only exhibits two types of zinc(II) ions, namely Zn1 and Zn2 (instead of four different zinc ions for compound **1**; see above).

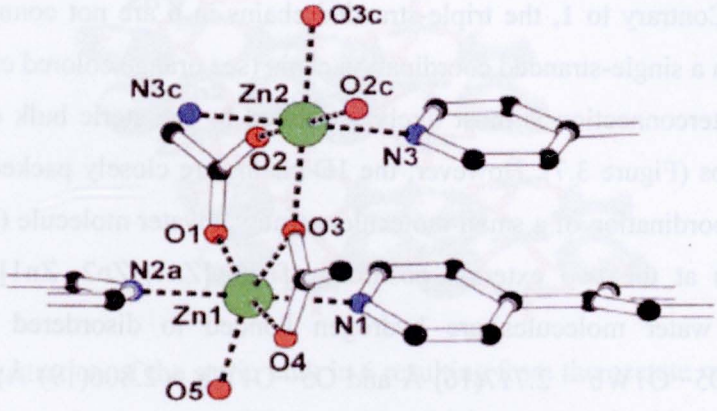

Figure 3.5 Representation of the asymmetric unit of **6** showing the atom labeling scheme for the zinc(II) ions. The hexafluoridophosphate anions, the lattice water molecules and the H atoms are not shown for clarity.

Zn1 is characterized by a strongly distorted octahedral coordination environment, owing to the small bite angle of the μ-O,O',O' bridging mode of one of the two acetato ligands (the angle O3–Zn1–O4 is only 58.34(12)°; Table 3.3). The basal plane is constituted of four oxygen atoms belonging to two acetato ligands (O1, O3 and O4) and one water molecule (O5). The octahedron is completed by two **4,4'-bpy** nitrogen atoms (N1 and N2a), at the axial positions. The Zn–O and Zn–N bond distances can be considered as normal for this type of ZnN_2O_4 coordination environment (Table 3.3).

Zn2 lies on an inversion centre. The coordination environment around the Zn2 ion is an almost perfect octahedron, since the basal angles, varying from 87.73(13) to 92.27(13)°, are close to the ideal value of 90°. At the basal plane, Zn2 is coordinated by four oxygen atoms (O2, O3, O2c and O3c) from different acetato ligands. The axial positions are occupied by nitrogen atoms N3 and N3c, belonging to two **4,4'-bpy** ligands (lying on an inversion centre) at common distances.

Zn2 is bridged to two symmetry-related Zn1 ions via two μ-O,O'- and two μ-O,O',O'-acetato ligands, generating a linear trinuclear [Zn1, Zn2, Zn1] cluster, analogous to the [Zn1, Zn3, Zn1] triad observed in **1** (see Figures 3.2 and 3.6).

The [Zn1, Zn2, Zn1] clusters are connected to each other through coordination of the zinc ions by **4,4'-bpy** ligands, producing a 1D chain, constituted of three single

zinc chains, indicated by the blue, green and yellow colored **4,4'-bpy** ligands in Figure 3.6. Contrary to **1**, the triple-stranded chains in **6** are not connected to each other through a single-stranded coordination chain (see orange colored chain in Figure 3.2). This interconnection is most likely prevented by the steric bulk of the acetato methyl groups (Figure 3.7). However, the 1D chains are closely packed, which only allows the coordination of a small molecule, namely a water molecule (O5 in Figures 3.6 and 3.7) at the two external positions of the [Zn1, Zn2, Zn1] triad. These coordinated water molecules are hydrogen bonded to disordered lattice water molecules (O5···O1Wb = 2.717(16) Å and O5···O1Wa = 2.806(19) Å). Similarly to the ClO_4^- ions in **1**, the PF_6^- anions occupy the voids in the crystal lattice of **6** and apparently do not play a significant role in the formation of the framework (since their only interactions occur with the disordered lattice water molecules; the F···O contact distances are in the range 2.89(3)–2.98(2) Å).

The crystal lattice is stabilized by hydrogen bonding between the oxygen atoms of neighboring acetato group with a O···O contact of 2.746(7) Å leading to the formation of the two- and three-dimensional structure (Figures 3.8 and 3.9).

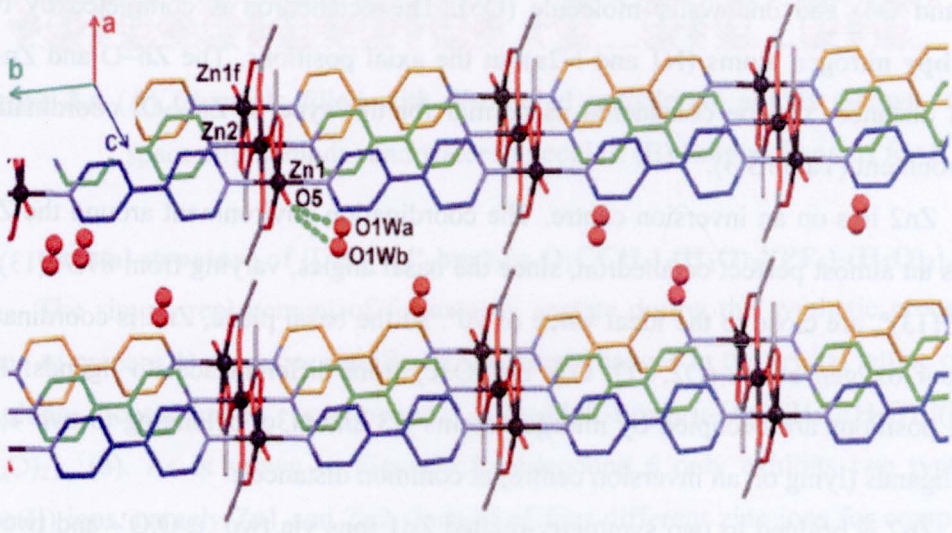

Figure 3.6 1D coordination network in **6** of Zn(II), 4,4'-bipyridine and acetate. The **4,4'-bpy** ligands involved in the formation of trinuclear zinc units are shown in blue, green and orange for comparison with compounds **1** and **7**.

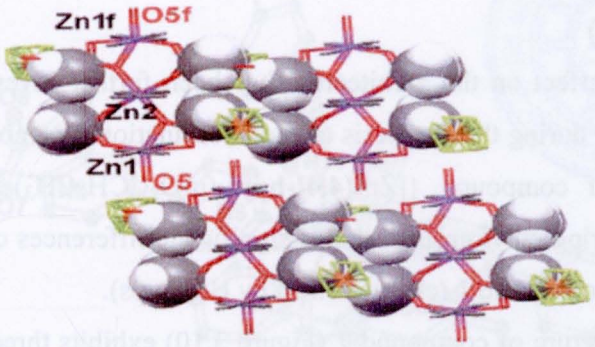

Figure 3.7 Illustration of the steric bulk in **6** resulting from the acetate methyl groups (shown in the space-filling mode), which prevents the interconnection of the triple-stranded chains.

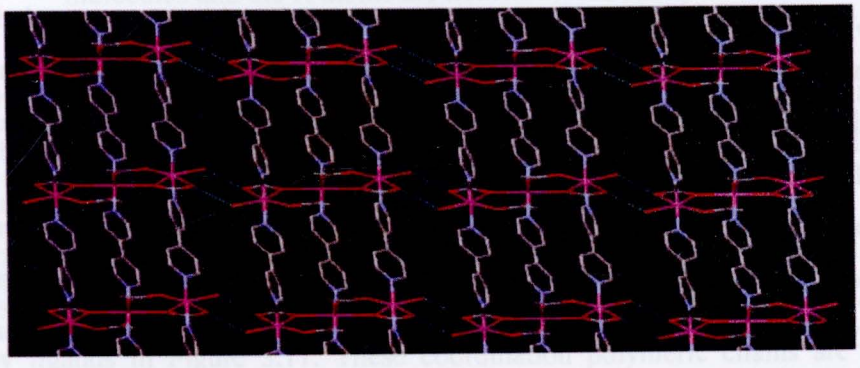

Figure 3.8 Packing diagram with hydrogen bond (dash-lines), showing the two-dimensional structure of **6.**

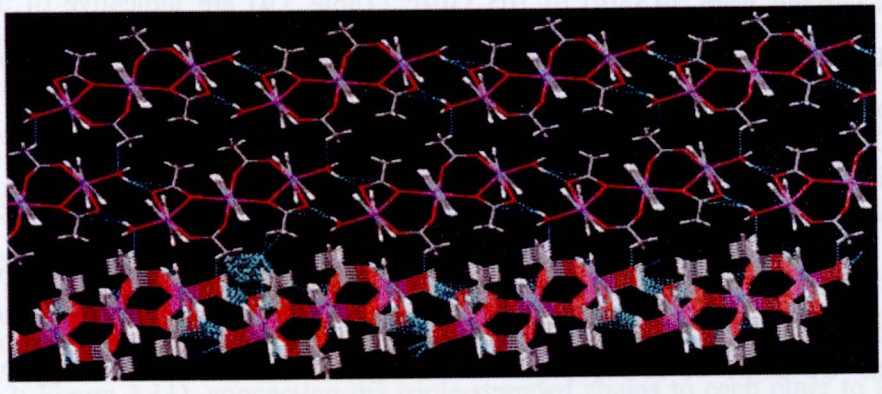

Figure 3.9 Packing diagram with hydrogen bond (dash-lines), showing the three-dimensional structure of **6**.

Crystal structure of $\{[Zn_3(4,4'\text{-bpy})_4(\mu\text{-}O_2CCH_2CH_3)_4](ClO_4)_2(4,4'\text{-bpy})_2(H_2O)_4\}_n$ (7)

The steric effect on the architecture has been further investigated by using a propionato ligand during the synthesis of the coordination assembly. Thus, the solid-state structure of compound $\{[Zn_3(\mathbf{4,4'\text{-bpy}})_4(\mu\text{-}O_2CCH_2CH_3)_4](ClO_4)_2(\mathbf{4,4'\text{-bpy}})_2(H_2O)_4\}_n$ (7), bearing ethyl groups, shows significant differences compared to that of **2** (holding CH_3 groups) and **1** (characterized by H groups).

The 2D structure of compound **7** (Figure 3.10) exhibits three different types of zinc(II) ions with octahedral N_2O_4 (Zn1) and N_3O_3 (Zn2, Zn3) geometries.

Zn1 exhibits an almost perfect octahedral environment with basal angles ranging from 89.22(9) to 91.47(9)° (Table 3.4). The basal plane is constituted of four oxygen atoms belonging to two μ-O,O'-propionato ligands (O2 and O6a) and two μ-O,O',O'-propionato ligands (O4 and O7a). The axial positions are occupied by two different **4,4'-bpy** ligands which connect Zn1 to symmetry-related Zn1 ions, generating a polymeric chain. The Zn–N and Zn–O bond lengths are comparable to those of the ZnN_2O_4 coordination units of the previous compounds.

Zn2 is coordinated at the basal plane of the octahedron by three oxygen atoms and one nitrogen atom from two propionato ligands (O3, O4 and O1) and one **4,4'-bpy** ligand (N11). The axial positions are occupied by two **4,4'-bpy** ligands (N3 and N5), linking Zn2 to two symmetry-related Zn3 ions, generating a polymeric chain exhibiting the sequence {Zn2, Zn3, Zn2, Zn3,...}. The Zn–O and Zn–N bond distances are in normal ranges for this type of coordination moiety.[24, 26] The basal angles varying from 59.55(9) to 105.33(9)° (Table 3.4) are indicative of a strong distortion of the octahedron, attributed to the small bite angle of the μ-O,O'-propionato ligand (O4–Zn2–O3 = 59.55(9)°).

The coordination environment around the Zn3 ion is comparable to that of Zn2. The ZnN_3O_3 unit exhibits analogous Zn–O and Zn–N bond lengths (to those of Zn2), which can be considered as normal (Table 3.4).[27] Similarly to Zn2, the coordination geometry around Zn3 is a strongly distorted octahedron, resulting from the small O7–Zn3–O8 angle of 59.57(9)° characterizing the coordination of the propionato ligand (Figure 3.10).

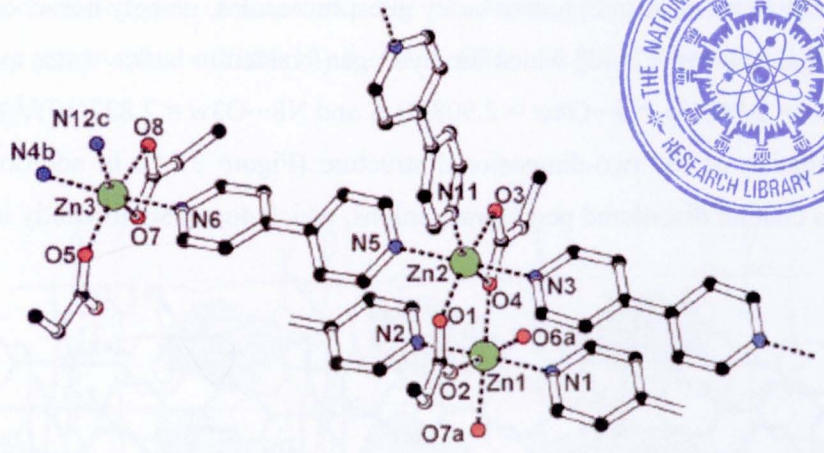

Figure 3.10 Representation of the asymmetric unit of **7** showing the atom labeling scheme for the zinc(II) ions. The perchlorate anions, the lattice water molecules and the H atoms are not shown for clarity.

The trinuclear [Zn1, Zn2, Zn1] clusters are connected to each other, in a head-to-tail fashion, through the coordination of the zinc ions by **4,4'-bpy** ligands, producing a 1D chain exhibiting the sequence {Zn1, Zn1, Zn1,...} for the central metal ion and { Zn2, Zn3, Zn2, Zn3,...} for the external zinc ions. This arrangement gives rise to triple-stranded chains, illustrated by the blue, green and yellow colored **4,4'-bpy** ligands in Figure 3.11. These coordination polymeric chains are closely related to those observed for compound **6** (see Figures 3.6 and 3.11) and resemble part of the network of compound **1** (see Figures 3.2 and 3.11). In contrast to the methyl groups in **6**, the ethyl groups of the propionato ligands in **7** do not allow a close packing of the triple-stranded polymeric chains (see Figures 3.7 and 3.12), as a result of steric constraints. Consequently, the trinuclear zinc(II) units in **7** are more separated from each other than those in **6** (Figures 3.7 and 10A). Indeed, the shorter intermolecular Zn···Zn separation distance is 9.391(3) Å for compound **7,** while the shorter intermolecular Zn···Zn distance is 5.557(3) Å for **6**.

This spatial organization allows the coordination of **4,4'-bpy** ligands at the two external positions of the trizinc moieties (orange **4,4'-bpy** ligands coordinated to Zn3 and Zn2; Figure 3.11), connecting the triple-stranded chains to each other to form a 2D network. The herringbone-type architecture (Figures 3.12A and 3.13) exhibits

large cavities that can accommodate bulky guest molecules, namely non-coordinated **4,4'-bpy** ligands (Figure 3.13) which are hydrogen-bonded to lattice water molecules (N10···O1w = 2.960(8), N9···O4w = 2.908(7) Å and N8···O3w = 2.827(10) Å) leading to the formation of the two-dimensional structure (Figure 3.14). In addition, these large voids contain disordered perchlorate anions, which do not significantly interact

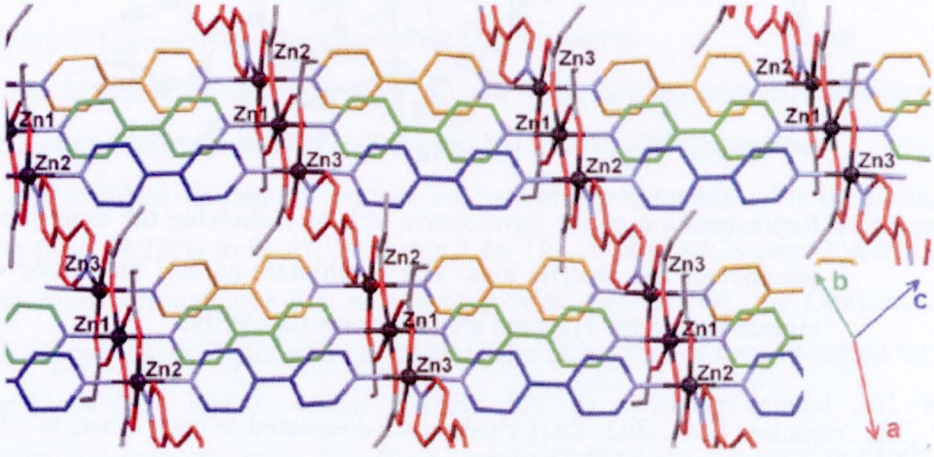

Figure 3.11 2D coordination network in **7** of Zn(II), 4,4'-bipyridine and propionate. The **4,4'-bpy** ligands involved in the formation of trinuclear zinc units are shown in blue, green and orange for comparison with compounds **1** and **6**. The **4,4'-bpy** ligands connecting 1D three-leg ladders are shown in red.

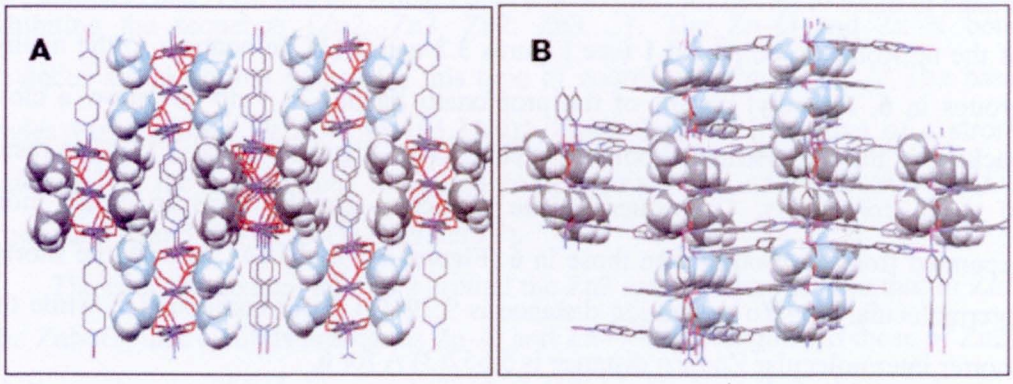

Figure 3.12 Illustrations of the steric hindrance originating from the propionato ethyl groups (shown in the space-filling mode, in grey and light blue) in **7**, which prevents close contacts between the 1D chains.

with the metal-organic framework, but are hydrogen bonded to lattice water molecules (O15···O2w = 2.889(12) Å, O12···O3w = 2.831(15) Å and O12b···O3w = 2.882(15) Å).

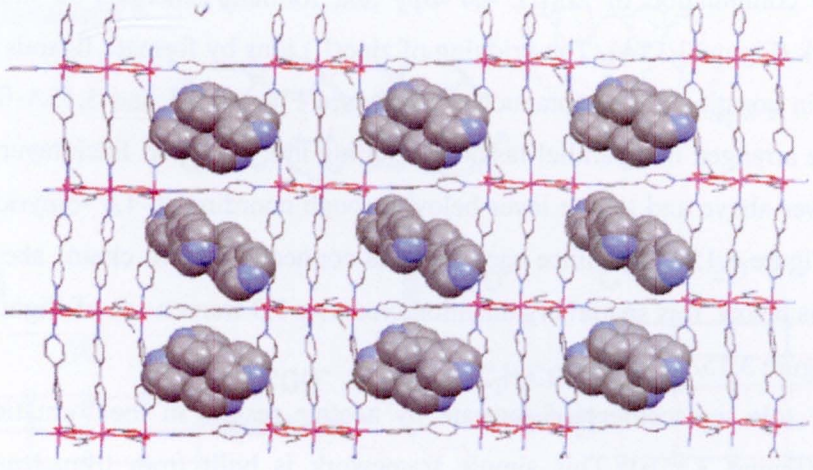

Figure 3.13 Representation of the 2D network of compound **7**, illustrating the large cavities which contain non-coordinated **4,4'-bpy** ligands (spacefilling mode).

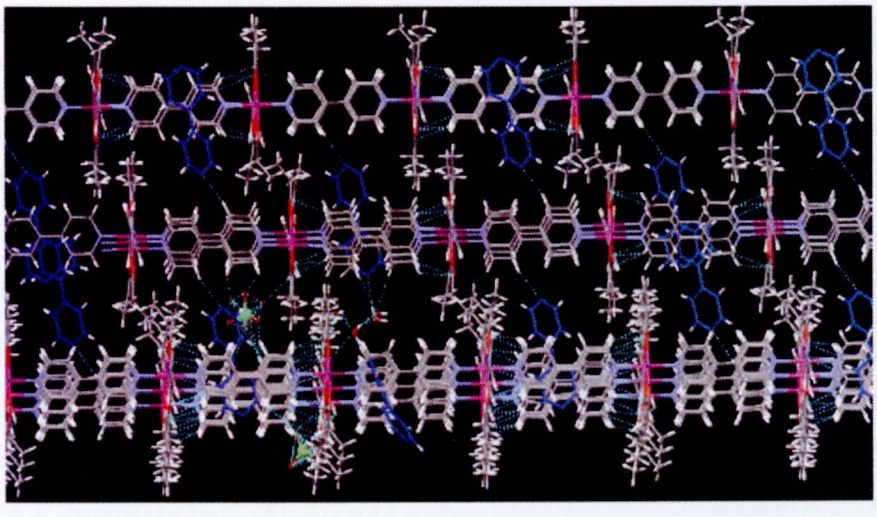

Figure 3.14 Packing diagram with hydrogen bond (dash-lines), showing the three-dimensional structure of **7**.

3.2.3 Effect of Carboxylate-regulator on Topologyies of 1, 6 and 7

The use of slightly different monocarboxylato moieties as secondary co-ligands of [Zn(II)/**4,4'-bpy**] coordination units, applying the same reaction conditions, leads to the formation of drastically distinct networks (Figure 3.15).

The combination of Zn(II), **4,4'-bpy** and formate generates an intricate 3D framework (Figure 3.15A). The bridging of zinc(II) ions by formato ligands produces a 1D chain constituted of heptanuclear rings (see Figures 3.3 and 3.15A-①). These chains are arranged in a parallel fashion, resulting in a 2D layer. Each layer is linked to one layer above and to one layer below through coordinated 4,4'-bipyridines (red lines in Figure 3.15A-②). Since each chain is connected to two chains above and to two chains below, this spatial organization creates a 3D framework of slightly shifted layers (Figure 3.15A-③).

The sole replacement of formate by acetate results in the formation of 1D network (Figure 3.15B). This simple framework is built from trinuclear acetato-bridged units that are linked to two adjacent ones, to form a three-leg ladder.

The use of propionate as co-ligand yields a 2D network (Figure 3.15C) which presents similarities with the previous one. Actually, the framework of **7** contains the three-leg ladders observed in solid-state structure of **6**. These three-leg ladders are connected to each other via **4,4'-bpy** ligands (vertical red lines in Figure 3.15C).

It should be noted that, despite the three coordination networks being different, they show some common features. Indeed, all three structures exhibit trinuclear carboxylato-bridged moieties as secondary building units (SBUs). Moreover, infinite $\{$–Zn–(**4,4'-bpy**)–$\}_n$ chains are observed for the three compounds (see for instance, the red colored $\{$–Zn4–(**4,4'-bpy**)–$\}_n$ chains in Figure 3.2, and the blue colored $\{$–Zn1/Zn2–(**4,4'-bpy**)–$\}_n$ chains in Figures 3.6 and 3.11, respectively). Finally, one should note that the zinc(II) ions have similar coordination environments, regardless of the carboxylato co-ligand used. Therefore, the structural diversity of the frameworks obviously originates from different steric constraints induced by the carboxylato ligands.

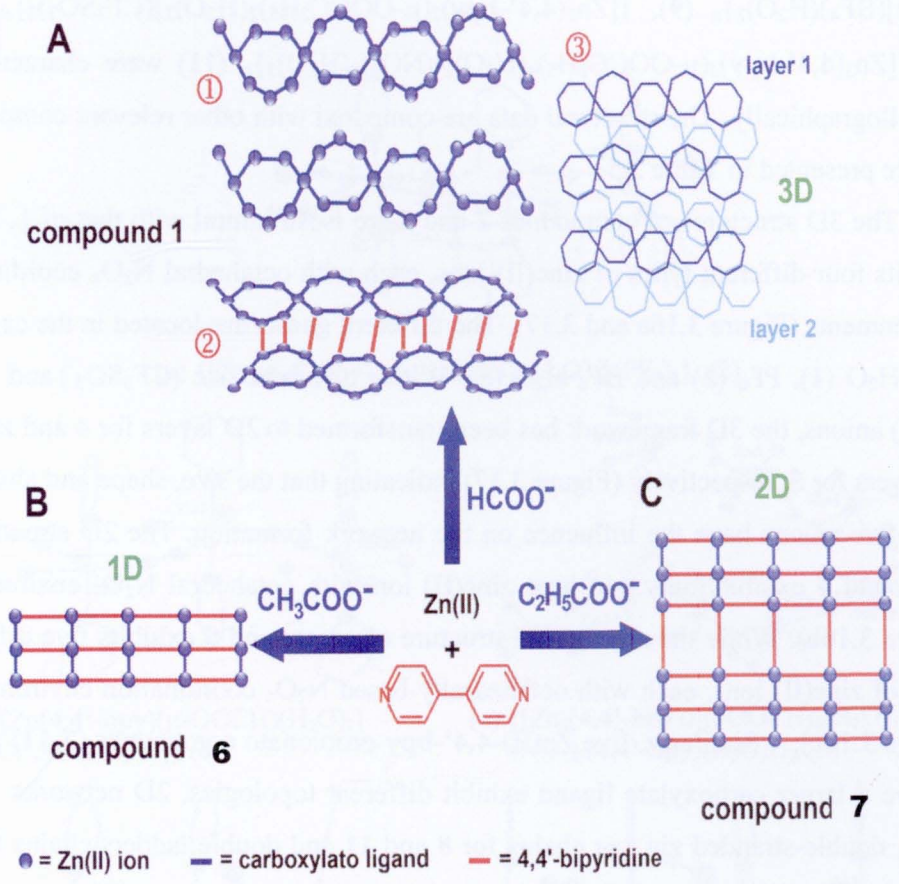

Figure 3.15 Coordination networks of A) compound **1** (3D), B) compound **6** (1D) and C) compound **7** (2D). A-①: 1D chains packed in a parallel fashion, forming a 2D layer; A-②: connection of two chains through **4,4'-bpy** ligands; A-③: packing of slightly shifted layers.

3.2.4 Comparison between the Frameworks of 1, 6 and 7 and Other Related Compounds

Eleven zinc(II)-**4,4'-bpy**-carboxylato compounds, $\{[Zn_3(\mathbf{4,4'\text{-}bpy})_{3.5}(\mu\text{-}OOCH)_4(H_2O)_2](X)_2\}_n$ when X = $ClO_4^-\cdot H_2O$ (**1**), PF_6^- (**2**), $BF_4^-\cdot H_2O$ (**3**), $\{[Zn(\mathbf{4,4'\text{-}bpy})(\mu\text{-}OOCH)(H_2O)_2](CF_3SO_3)(H_2O)\}_n$ (**4**), $\{[Zn_4(\mathbf{4,4'\text{-}bpy})_4(\mu\text{-}OOCH)_5(H_2O)_5](NO_3)_3(\mathbf{4,4'\text{-}bpy})_2(H_2O)_3\}_n$ (**5**), $\{[Zn_3(\mathbf{4,4'\text{-}bpy})_3(\mu\text{-}OOCCH_3)_4(H_2O)_2](PF_6)_2(H_2O)_2\}_n$ (**6**), $\{[Zn_3(\mathbf{4,4'\text{-}bpy})_4(\mu\text{-}OOCCH_2CH_3)_4](ClO_4)_2(\mathbf{4,4'\text{-}bpy})_2(H_2O)_4\}_n$ (**7**), $\{[Zn_3(\mathbf{4,4'\text{-}bpy})_4(\mu\text{-}OOCC_2H_5)_4(H_2O)_2](PF_6)_2(H_2O)_2\}_n$ (**8**), $\{[Zn_2(\mathbf{4,4'\text{-}bpy})_2(\mu\text{-}OOCC_2H_5)_2(OH)$

$(H_2O)](BF_4)(H_2O)_2\}_n$ (**9**), $\{[Zn_2($**4,4'-bpy**$)_2(\mu\text{-}OOCC_2H_5)_2(H_2O)_2](CF_3SO_3)_2\}_n$ (**10**), and $\{[Zn_3($**4,4'-bpy**$)_4(\mu\text{-}OOCC_2H_5)_4(H_2O)_2](NO_3)_2(H_2O)_3\}_n$ (**11**) were characterized crystallographically. The structural data are compared with other relevant compounds and are presented in Table 3.5.

The 3D structures of compounds **2** and **3** are isostructural with that of **1,** which exhibits four different types of zinc(II) ions, each with octahedral N_2O_4 coordination environments (Figure 3.16a and 3.17). The different guests are located in the cavities, $ClO_4{\bullet}H_2O$ (**1**), PF_6 (**2**) and $BF_4{\bullet}H_2O$ (**3**). With a different size ($CF_3SO_3^-$) and shape (NO_3^-) anions, the 3D framework has been transformed to 2D layers for **4** and zig zag 2D layers for **5**, respectively (Figure 3.17) indicating that the size, shape and ability of these five anions have the influence on the network formation. The 2D structure of compound **4** exhibits only one type zinc(II) ion with octahedral N_2O_4 environment (Figure 3.16b). While the zig zag 2D structure of compound **5** exhibits five different types of zinc(II) ions, each with octahedrally-based N_2O_4 coordination environments (Figure 3.16c). Similarly, five Zn(II)-**4,4'-bpy**-propionato compounds (**7-11**) which involve a larger carboxylate ligand exhibit different topologies, 2D networks for **7** and **9**, double-stranded zig zag chains for **8** and **11** and double ladders chains for **10** (Figure 3.17). The 1D structure of compound **8** is isostructural to **11** (Figures 3.16d and g), which exhibits three different types of zinc(II) ions with octahedrally based N_2O_4 geometries. The different guests are filled in the channels for $PF_6{\bullet}H_2O$ (**8**) and $NO_3{\bullet}H_2O$ (**11**). Each Zn(II) is characterized by a distorted octahedral coordination environment. The feature of the zig zag double-stranded chains is very comparable to the triple-stranded chains of **6** (Figure 3.6) in which the axial positions of octahedron of two external positions are completed by two **4,4'-bpy** nitrogen atoms (Figure 3.6) generating a triple-stranded chains, while two external positions of the trizinc moities of **7** (Figure 3.11) connect the triple-stranded chains to each other to form a 2D network. The 2D structure of compound **9** exhibits two different types of zinc(II) ions, each with octahedral N_2O_4 coordination environments (Figure 3.16e). While the 1D structure of compound **10** involves dimer unit of zinc(II) ions. Each Zn(II) is characterized by a distorted trigonal bipyramidal geometry (Figure 3.16f).

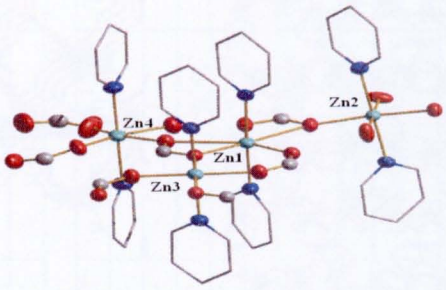

(a) $\{[Zn_3(\mathbf{4,4'\text{-}bpy})_{3.5}(\mu\text{-}OOCH)_4(H_2O)_2](PF_6)_2\}_n$ (**2**)

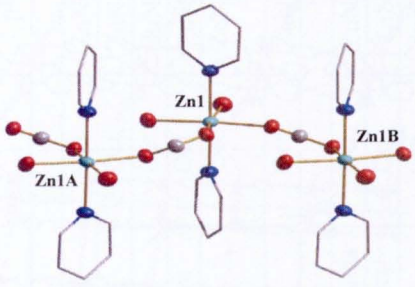

(b) $\{[Zn(\mathbf{4,4'\text{-}bpy})(\mu\text{-}OOCH)(H_2O)_2](CF_3SO_3)(H_2O)\}_n$ (**4**)

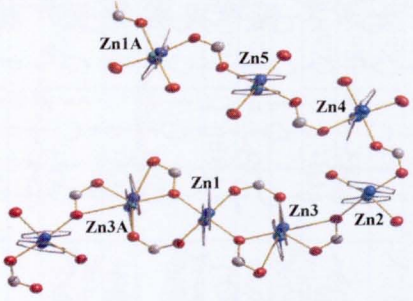

(c) $\{[Zn_4(\mathbf{4,4'\text{-}bpy})_4(\mu\text{-}OOCH)_5(H_2O)_5](NO_3)_3(\mathbf{4,4'\text{-}bpy})(H_2O)_6\}_n$ (**5**)

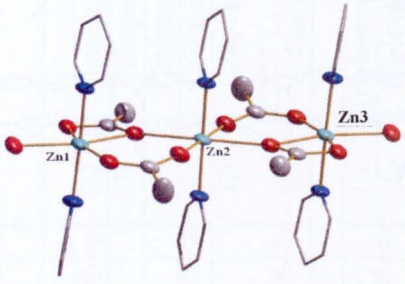

(d) $\{[Zn_3(\mathbf{4,4'\text{-}bpy})_4(\mu\text{-}OOCC_2H_5)_4(H_2O)_2](PF_6)_2(H_2O)_2\}_n$ (**8**)

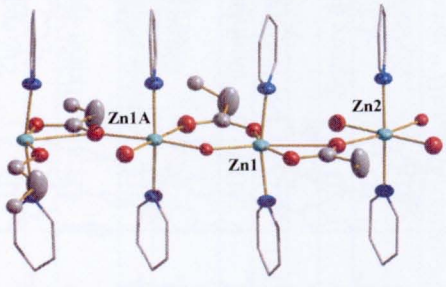

(e) $\{[Zn_2(\mathbf{4,4'\text{-}bpy})_2(\mu\text{-}OOCC_2H_5)_2(OH)(H_2O)](BF_4)(H_2O)_2\}_n$ (**9**)

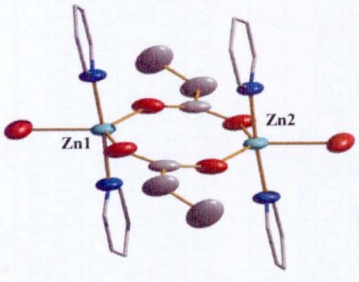

(f) $\{[Zn_2(\mathbf{4,4'\text{-}bpy})_2(\mu\text{-}OOCC_2H_5)_2(H_2O)_2](CF_3SO_3)_2\}_n$ (**10**)

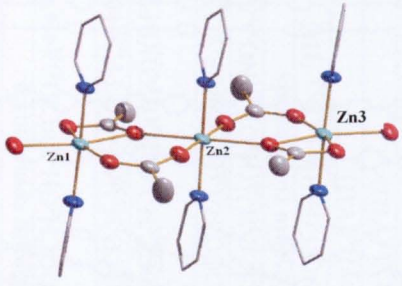

(g) $\{[Zn_3(\mathbf{4,4'\text{-}bpy})_4(\mu\text{-}OOCC_2H_5)_4(H_2O)_2](NO_3)_2(H_2O)_3\}_n$ (**11**)

Figure 3.16 The structures of zinc(II)-**4,4'-bpy**-carboxylato compounds **2-5** and **8-11**.

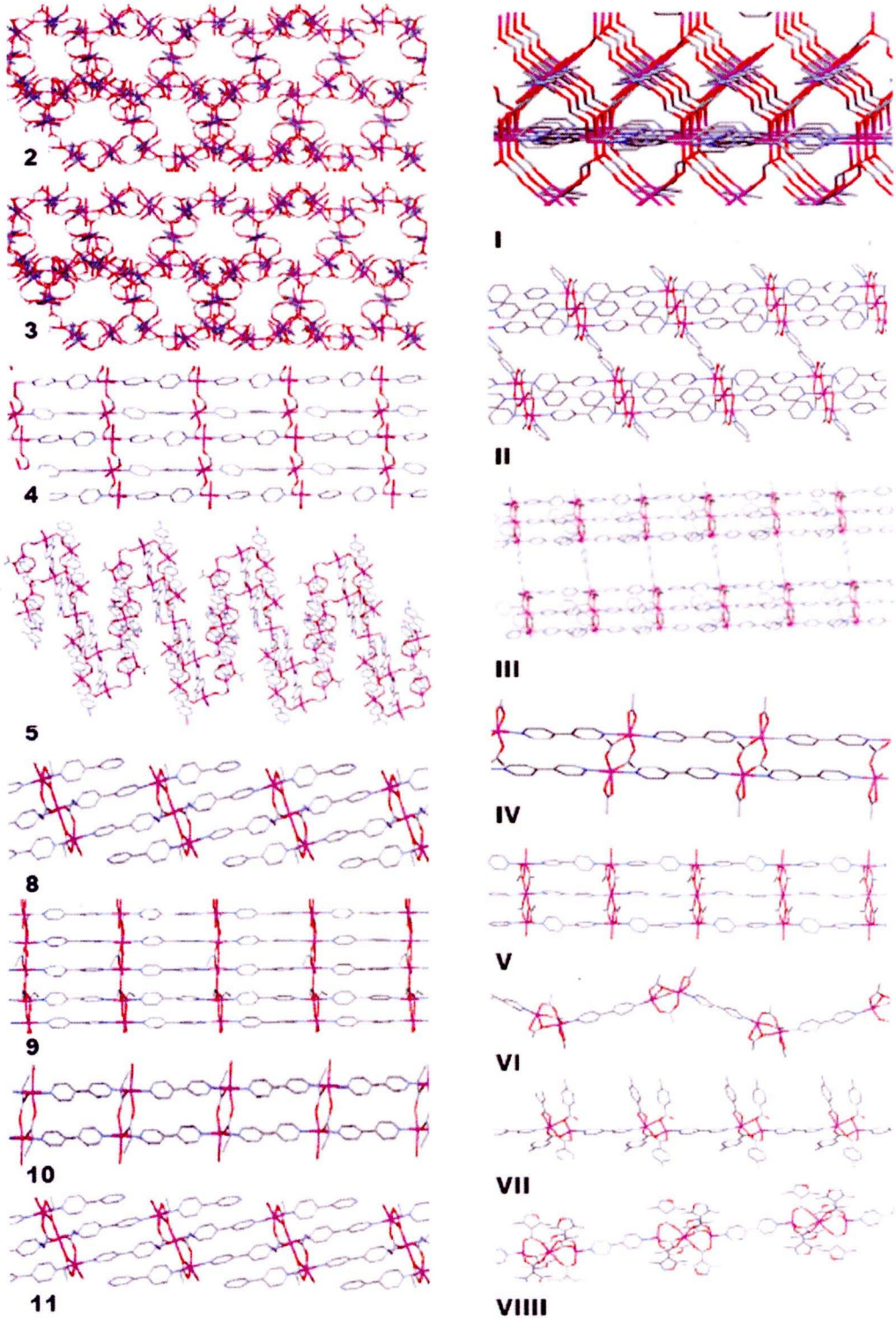

Figure 3.17 Representations of the related structure of some [Zn(II)/**4,4'-bpy**/ carboxylato]-based coordination networks.

Table 3.5 Structural descriptions for [Zn(II)/**4,4'-bpy**/carboxylato]-based coordination networks.

Compound	Type	Topology	Geometry	Chromo phore	Mode of (-OCO-)	Reference
Zn(II)/4,4'-bpy/formato compounds						
$\{[Zn_3(\mathbf{4,4'\text{-}bpy})_{3.5}(\mu\text{-}OOCH)_4(H_2O)_2](ClO_4)_2(H_2O)_2\}_n$ (**1**)	3D	Interpenetrating	Oct.	$ZnN_2O_2O_2'$	$\mu\text{-}\eta^1\text{-}\eta^1$; $\mu_3\text{-}\eta^2\text{-}\eta^1$	This work
$\{[Zn_3(\mathbf{4,4'\text{-}bpy})_{3.5}(\mu\text{-}OOCH)_4(H_2O)_2](PF_6)_2\}_n$ (**2**)	3D	Interpenetrating	Oct.	$ZnN_2O_2O_2'$	$\mu\text{-}\eta^1\text{-}\eta^1$; $\mu_3\text{-}\eta^2\text{-}\eta^1$	This work
$\{[Zn_3(\mathbf{4,4'\text{-}bpy})_{3.5}(\mu\text{-}OOCH)_4(H_2O)_2](BF_4)_2(H_2O)_2\}_n$ (**3**)	3D	Interpenetrating	Oct.	$ZnN_2O_2O_2'$	$\mu\text{-}\eta^1\text{-}\eta^1$; $\mu_3\text{-}\eta^2\text{-}\eta^1$	This work
$\{[Zn(\mathbf{4,4'\text{-}bpy})(\mu\text{-}OOCH)(H_2O)_2](CF_3SO_3)(H_2O)\}_n$ (**4**)	2D	Square qrid layers	Oct.	$ZnN_2O_2O_2'$	$\mu\text{-}\eta^1\text{-}\eta^1$	This work
$\{[Zn_4(\mathbf{4,4'\text{-}bpy})_4(\mu\text{-}OOCH)_5(H_2O)_5](NO_3)_3(\mathbf{4,4'\text{-}bpy})(H_2O)_6\}_n$ (**5**)	2D	Zig-zag layers	Oct.	$ZnN_2O_2O_2'$	$\mu\text{-}\eta^1\text{-}\eta^1$; $\mu\text{-}\eta^2\text{-}\eta^1$	This work
$[Zn(\mathbf{4,4\text{-}bipy})(OOCH)_2(C_{10}H_8N_2)]_n$ (**I**)	3D	Framework	Oct.	$ZnN_2O_2O_2'$	$\mu\text{-}\eta^1\text{-}\eta^1$	83
Zn(II)/4,4'-bpy/acetato compounds						
$\{[Zn_3(\mathbf{4,4'\text{-}bpy})_3(\mu\text{-}OOCCH_3)_4(H_2O)_2](PF_6)_2(H_2O)_2\}_n$ (**6**)	1D	Triple-stranded chains	Oct.	$ZnN_2O_2O_2'$	$\mu\text{-}\eta^1\text{-}\eta^1$; $\mu\text{-}\eta^2\text{-}\eta^1$	This work
$[Zn_3(\mathbf{4,4'\text{-}bpy})_4(OAc)_4](ClO_4)_2(H_2O)_2$ (**II**)	2D	Triple chain sheets	Oct.	ZnN_3O_2O'	$\mu\text{-}\eta^2\text{-}\eta^1$	84
$[Zn(\mathbf{4,4'\text{-}bipy})(AcO)_2]$ (**IV**),	1D	Double ladders	Oct.	$ZnN_2O_2O_2'$	$\mu\text{-}\eta^1\text{-}\eta^1$	86
$[Zn_3(\mathbf{4,4'\text{-}bpy})_3(OAc)_4(H_2O)_2](ClO_4)_2(H_2O)$ (**V**),	1D	Three-leg ladders	Oct.	$ZnN_2O_2O_2'$	$\mu\text{-}\eta^1\text{-}\eta^1$; $\mu\text{-}\eta^2\text{-}\eta^1$	84
$[Zn_2(\mathbf{4,4'\text{-}bpy})(OAc)_4]$n (**VI**),	1D	Zig-zag chains	Oct.	$ZnN_2O_2O_2'$	$\mu\text{-}\eta^1\text{-}\eta^1$; $\mu\text{-}\eta^2\text{-}\eta^1$	87
Zn(II)/4,4'-bpy/propionato compounds						
$\{[Zn_3(\mathbf{4,4'\text{-}bpy})_4(\mu\text{-}OOCCH_2CH_3)_4](ClO_4)_2(\mathbf{4,4'\text{-}bpy})_2(H_2O)_4\}_n$ (**7**)	2D	Triple chain sheets	Oct.	ZnN_3O_2O'	$\mu\text{-}\eta^1\text{-}\eta^1$; $\mu\text{-}\eta^2\text{-}\eta^1$	This work
$\{[Zn_3(\mathbf{4,4'\text{-}bpy})_4(\mu\text{-}OOCC_2H_5)_4(H_2O)_2](PF_6)_2(H_2O)_2\}_n$ (**8**)	1D	Doble-stranded ladders	Oct.	$ZnN_2O_2O_2'$	$\mu\text{-}\eta^1\text{-}\eta^1$; $\mu\text{-}\eta^2\text{-}\eta^1$	This work
$\{[Zn_2(\mathbf{4,4'\text{-}bpy})_2(\mu\text{-}OOCC_2H_5)_2(OH)(H_2O)](BF_4)(H_2O)_2\}_n$ (**9**)	2D	Zig-zag layers	Oct.	$ZnN_2O_2O_2'$	$\mu\text{-}\eta^1\text{-}\eta^1$; $\mu\text{-}\eta^2\text{-}\eta^1$	This work
$\{[Zn_2(\mathbf{4,4'\text{-}bpy})_2(\mu\text{-}OOCC_2H_5)_2(H_2O)_2](CF_3SO_3)_2\}_n$ (**10**)	1D	Double ladders	TBP	ZnN_2O_2O'	$\mu\text{-}\eta^1\text{-}\eta^1$	This work
$\{[Zn_3(\mathbf{4,4'\text{-}bpy})_4(\mu\text{-}OOCC_2H_5)_4(H_2O))_2](NO_3)_2(H_2O)_3\}_n$ (**11**)	1D	Doble-stranded ladders	Oct.	$ZnN_2O_2O_2'$	$\mu\text{-}\eta^1\text{-}\eta^1$; $\mu\text{-}\eta^2\text{-}\eta^1$	This work
Zn(II)/4,4'-bpy/carboxylato compounds						
$[Zn_3(4,4'\text{-}bpy)_4(pa)_4](NO_3)_2(paH)(H_2O)_{2.5}$ (**III**)	2D	Square qrid layers	Oct.	$ZnN_2O_2O_2'$	$\mu\text{-}\eta^1\text{-}\eta^1$; $\mu\text{-}\eta^2\text{-}\eta^1$	85
$[Zn_2(C_8H_7O_2)_4(\mathbf{4,4'\text{-}bpy})]_n$ (**VII**)	1D	Chains	Oct.	$ZnN_2O_2O_2'$	$\mu\text{-}\eta^1\text{-}\eta^1$; $\mu\text{-}\eta^2\text{-}\eta^1$	88
$[Zn_3(DMIC)_6(\mathbf{4,4'\text{-}bpy})]_n$ (**VIII**)	1D	Zig-zag chains	Oct.	$ZnN_2O_2O_2'$	$\mu\text{-}\eta^1\text{-}\eta^1$	89

4,4'-bpy = 4,4'-bipyridine; DMIC = 3,5-dimethylisoxazole-4-carboxylate; paH = phenylacetic acid; $C_8H_7O_2$ = 4-methylbenzoato; TBP = distorted trigonal bipyramidal; Oct. = distorted octahedral.

Eight previously reported coordination frameworks exclusively constructed from zinc(II) ions, 4,4'-bipyridine ligands and bridging carboxylato units are listed in Table 3.5. In these the zinc(II) ions are bridged through carboxylate bridging ligands with the three-dimensional structure $[Zn(OOCH)_2(\mathbf{4,4'\text{-}bpy})]_n$ **(I)**,[83] the two-dimensional structures $\{[Zn_3(\mathbf{4,4'\text{-}bpy})_4(OAc)_4](ClO_4)_2(H_2O)_2\}_n$ **(II)**[84] and $\{[Zn_3(\mathbf{4,4'\text{-}bpy})_4(pa)_4](NO_3)_2(paH)(H_2O)_{2.5}\}_n$ **(III)**[85] (paH = phenylacetic acid), and the one-dimensional structures $[Zn(\mathbf{4,4'\text{-}bipy})(AcO)_2]_n$ **(IV)**,[86] $\{[Zn_3(\mathbf{4,4'\text{-}bpy})_3(OAc)_4(H_2O)_2](ClO_4)_2(H_2O)\}_n$ **(V)**,[90] $[Zn_2(\mathbf{4,4'\text{-}bpy})(OAc)_4]_n$ **(VII)**,[87] $[Zn_2(C_8H_7O_2)_4(\mathbf{4,4'\text{-}bpy})]_n$ **(VII)**[88] and $[Zn_3(DMIC)_6(\mathbf{4,4'\text{-}bpy})]_n$ **(VIII)**[89] (DMIC = 3,5-dimethyl isoxazole-4-carboxylate). Representations of these frameworks are shown in Figure 3.17. From the eight compounds, three, *i.e.* **II**, **III** and **V**, show frameworks that are comparable to those of **6** and **7**. Actually, as already mentioned above, compound **V** is isostructural to **6**. The sole difference between **V** and **6** lies in the distinct lattice anions, ClO_4^- and PF_6^-, respectively. This demonstrates that the two anions have no influence on the network formation. The 2D triple-chain sheet architectures of **II**[84] and **III**[85] are comparable to that of **7**. The remaining four compounds exhibit 1D networks (**IV**, **VI-VIII**). Interestingly, only **I** exhibits a 3D structure with formato co-ligands. This behavior is also observed in the present study, i.e. the formation of 3D networks in the case of **1-3** when formate is used as a secondary ligand. Therefore, the lower steric hindrance exerted by the formato ligand appears to favor the formation of 3D structures. Finally, it has to be noted that all carboxylato units act as bridging ligands, linking two or three zinc(II) atoms. The resulting zinc clusters are further connected to each other through the 4,4'-bipyridine ligands generating the higher-dimension frameworks.

3.3 Physical Properties

3.3.1 Thermogravimetric Properties

The thermal decomposition behavior of compound **1** (Figure 3.18A) reveals a first weight loss in the temperature range 143–201 °C, corresponding to four water molecules (experimental value, 5.50%; calculated, 6.03%). Above 202 °C, compound **1** starts to decompose. When **1** is heated up to 800 °C, a white residue is obtained, which is most likely ZnO as deduced from the weight loss.

The thermogravimetric analysis of compound **6** (Figure 3.18F) shows a first weight loss in the temperature range 71–170 °C, characteritheistic for the loss of four water molecules (experimental value, 5.82%; calculated, 5.70%). In the temperature range 171–429 °C, the decomposition of the coordination material is observed.

The thermal analysis of **7** (Figure 3.18G) exhibits a two-stage decomposition of the material. A first weight loss of 3.50% is observed in the temperature range 92–195 °C, which corresponds to the release of four lattice water molecules (calculated 4.15%). In the temperature range 196–630 °C, compound **7** degrades. As for compounds **1** and **6**, a white residue (ZnO) is obtained when the sample is heated to 800 °C.

The thermal behavior of the remaining compounds is given in Figure 3.18. The thermogravimetric analysis of **2-5** first weight loss in the temperature range 71–170 °C, characterizing the loss of the water molecules (experimental value, 3.01% (**2**), 6.28% (**3**), 7.61% (**4**), and 8.07% (**5**); calculated, 2.88% (**2**), 6.16% (**3**), 7.66% (**4**), and 8.21% (**5**)). In the other hand the thermal analysis of **8-11** shows two weight losses of water molecules in the temperature range 143–201 °C, corresponding to four water molecules (experimental value, 4.94% (**8**), 7.46% (**9**), 3.54% (**10**), and 11.57% (**11**); calculated, 4.87% (**8**), 7.23% (**9**), 3.80% (**10**), and 10.85% (**11**)). The final product of the thermal decomposition of all compounds is a white powder that appears to be a white residue (ZnO).

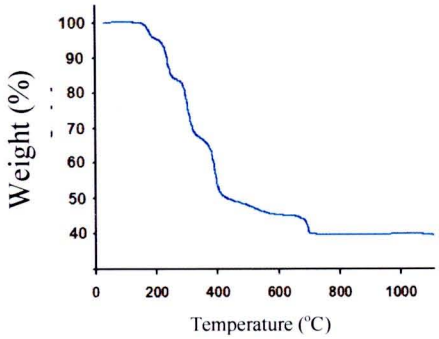

(a) $\{[Zn_3(\mathbf{4,4'\text{-}bpy})_{3.5}(\mu\text{-}OOCH)_4(H_2O)_2](ClO_4)_2(H_2O)_2\}_n$ (**1**)

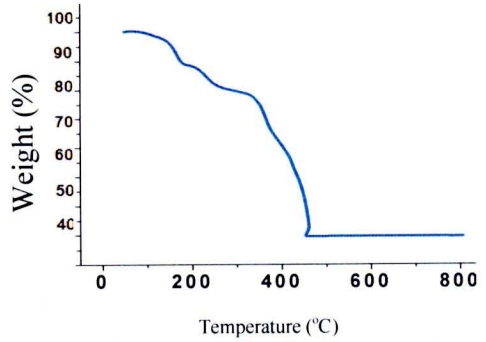

(b) $\{[Zn_3(\mathbf{4,4'\text{-}bpy})_{3.5}(\mu\text{-}OOCH)_4(H_2O)_2](PF_6)_2\}_n$ (**2**)

Figure 3.18 (a)-(k) Thermogravimetric analysis of compounds **1-11**.

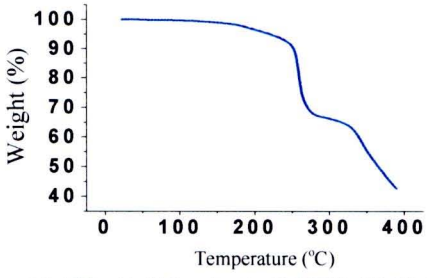

(c) $\{[Zn_3(\mathbf{4,4'\text{-}bpy})_{3.5}(\mu\text{-}OOCH)_4(H_2O)_2](BF_4)_2(H_2O)_2\}_n$ (**3**)

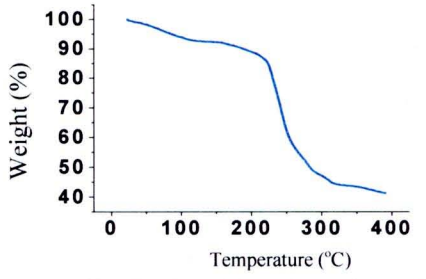

(d) $\{[Zn(\mathbf{4,4'\text{-}bpy})(\mu\text{-}OOCH)(H_2O)_2](CF_3SO_3)(H_2O)\}_n$ (**4**)

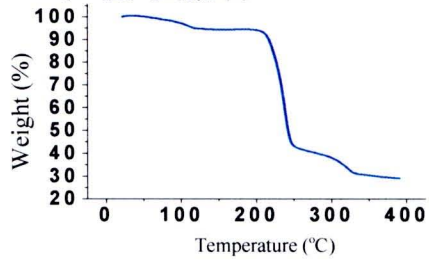

(e) $\{[Zn_4(\mathbf{4,4'\text{-}bpy})_4(\mu\text{-}OOCH)_5(H_2O)_5](NO_3)_3(\mathbf{4,4'\text{-}bpy})(H_2O)_6\}_n$ (**5**)

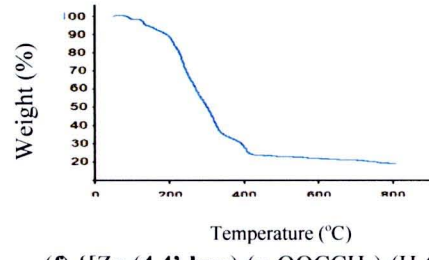

(f) $\{[Zn_3(\mathbf{4,4'\text{-}bpy})_3(\mu\text{-}OOCCH_3)_4(H_2O)_2](PF_6)_2(H_2O)_2\}_n$ (**6**)

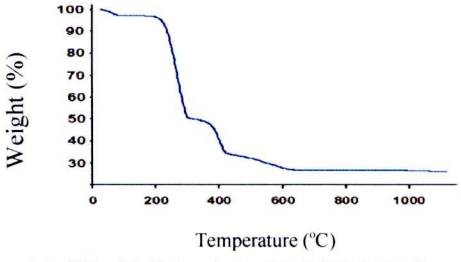

(g) $\{[Zn_3(\mathbf{4,4'\text{-}bpy})_4(\mu\text{-}OOCCH_2CH_3)_4](ClO_4)_2(\mathbf{4,4'\text{-}bpy})_2(H_2O)_4\}_n$ (**7**)

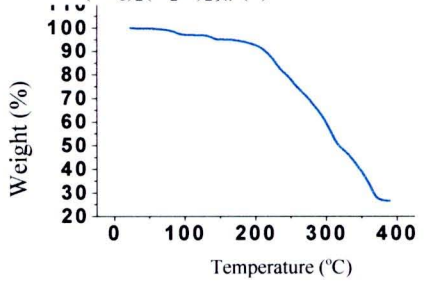

(h) $\{[Zn_3(\mathbf{4,4'\text{-}bpy})_4(\mu\text{-}OOCC_2H_5)_4(H_2O)_2](PF_6)_2(H_2O)_2\}_n$ (**8**)

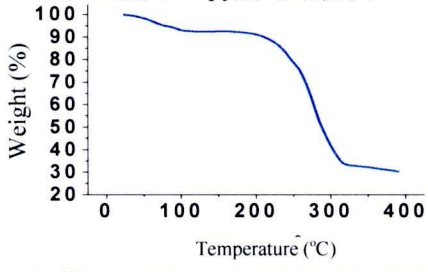

(i) $\{[Zn_2(\mathbf{4,4'\text{-}bpy})_2(\mu\text{-}OOCC_2H_5)_2(OH)(H_2O)](BF_4)(H_2O)_2\}_n$ (**9**)

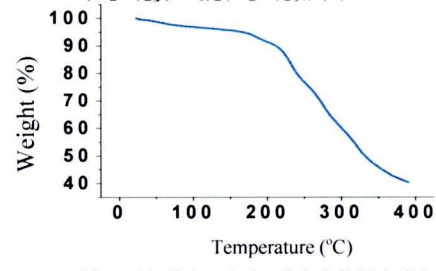

(j) $\{[Zn_2(\mathbf{4,4'\text{-}bpy})_2(\mu\text{-}OOCC_2H_5)_2(H_2O)_2](CF_3SO_3)_2\}_n$ (**10**)

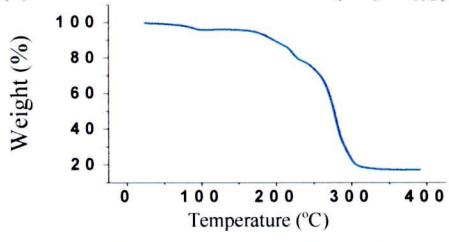

((k) $\{[Zn_3(\mathbf{4,4'\text{-}bpy})_4(\mu\text{-}OOCC_2H_5)_4(H_2O)_2](NO_3)_2(H_2O)_3\}_n$ (**11**)

Figure 3.18 (a)-(k) Thermogravimetric analysis of compounds **1-11 (Cont.)**.

3.3.2 Luminescent Properties

The free carboxylate (formate, acetate and propionate) ligands show no emission in the visible region, whereas the **4,4'-bpy** ligand shows a fluorescent emission band at λ_{max} = 437 nm ($\lambda_{excitation}$ = 254 nm). Upon coordination of the two types of ligands with the zinc(II) ion, all Zn(II)-**4,4'-bpy**-carboxylato compounds (excited at 254 nm) display a strong violet fluorescent emission band in the solid state n the range λ_{max} = 380-386 nm for **1-11** (Figure 3.19 for **1**, **6** and **7** and Appendix C for the remaining compounds). The emission spectra of all compounds were assigned primarily to ligand-to-metal charge transfer (LMCT).[90] The fluorescent intensity of all compounds are higher than the free **4,4'-bpy** ligand, which can be attributed to the coordination of the **4,4'-bpy** ligands to zinc(II) ions, which effectively increases the rigidity of the **4,4'-bpy** ligand and reduces the loss of energy via radiationless decay of the intraligand emission excited state. [90]

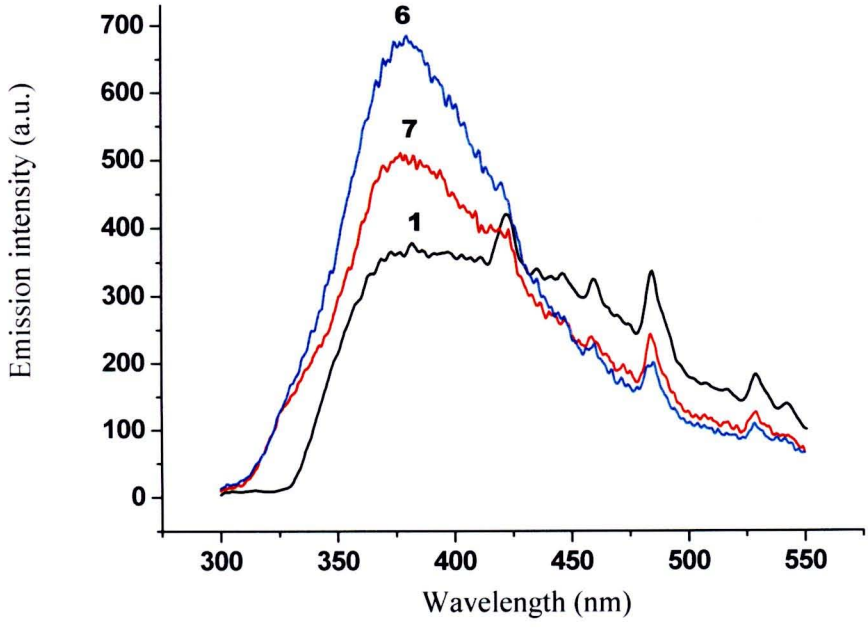

Figure 3.19 The solid-state fluorescent spectra of compounds **1**, **6** and **7** in arbitrary units.

3.4 Potential Cation-exchange Properties with Structure Retention by Doping Zn(II) Compounds with Cu(II) and Mn(II)

All doped compounds were prepared in a similar manner as the original zinc(II) compounds, but with doping amounts of paramagnetic metal ions, Cu(II) and Mn(II) to investigate the cation-exchange behavior of the materials, and analyze the coordination environment around the Zn(II) ions. The preparations were performed in ethanol/H_2O, or methanol/H_2O, using solution Zn(II)/Cu(II) and Zn(II)/Mn(II) ratios of 95:5. All doped compounds have been characterized by XRPD, IR and EPR at RT and 70 K (see Appendix B). The XRPD patterns and IR spectra of the doped compounds are similar to that of the original Zn(II) compounds, thus indicating that the structure and therefore the environment around the zinc(II) centers are not altered.

For instance, the polycrystalline EPR spectrum of the trinuclear Zn(II) compound **6** doped with Cu(II) shows signals revealing the presence of two different types of Cu(II) species. Each one is characterized by a four-lines hyperfine pattern with $g_{//} = 2.343$ and 2.275; (with $A_{//} = 124$ and 126; red and blue dots in Figure 3.20a) $g_{\perp} = 2.094$ and 2.094 in agreement with a distorted-octahedral geometry.[91] No super-hyperfine splitting is resolved. These EPR data are clearly indicative of the occurrence of two different environments for the Zn(II) ions in **6**, which have been replaced by Cu(II) ions. Actually, a close observation of the structure of **6** clearly reveals the presence of two distinct coordination geometries for the zinc ions, a highly distorted octahedron (site I in Figure 3.20b) and an almost perfect octahedron (site II in Figure 3.20b). Each trinuclear zinc unit in **6** is formed by two external sites (I) and one central site (II).

The doping with Mn(II) ions leads to a heteronuclear compound, whose EPR spectrum shows only one set of six lines, characterizing a Mn(II) species (Figure 3.20c). These data suggest that only one from the two potential coordination sites has experienced ion exchange. Most likely Mn(II) ions are only capable of occupying site (II) (Figure 3.20d), since Mn(II) has the tendency to form regular octahedral compounds. The polycrystalline EPR spectra of **1** and **7** as well as the remaining compounds doped with Cu(II) and Mn(II) exhibit similar features, thus suggesting comparable ion-exchange properties (see Appendix B).

The influence of the nature of the doping metal ion, namely Cu(II) and Mn(II), has been successfully investigated by EPR. This study illustrates the flexibility of the coordination geometry of Cu(II) compared to Mn(II). Such investigations are of great interest in the context of potential cation-exchange properties of MOFs with structure retention.

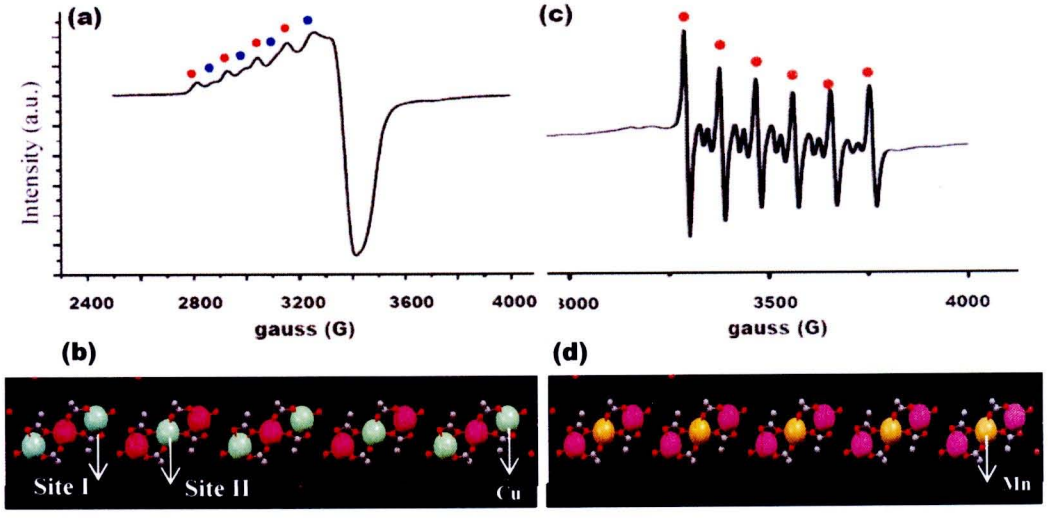

Figure 3.20 (a) Polycrystalline EPR spectrum of **6** doped with Cu(II), recorded at 70 K. The two species are illustrated by blue and red dots. (b) Trinuclear Zn(II) units of **6** where zinc(II) ions (pink) have been replaced by Cu(II) ions (green) in two different sites (sites I and II). (c) Polycrystalline EPR spectrum of **6** doped with Mn(II), recorded at 70 K and (d) trinuclear Zn(II) unit of **6,** where only the central Zn(II) sites have been replaced by Mn(II) ions.

3.5 Dynamic Structural Transformation

The single-crystal X-ray structures of **1, 3-9** and **11** reveal the presence of lattice water molecules, indicating a potential porosity of the materials. Thus, all room-temperature stable compounds exhibit open channels that are occupied by guest water molecules. The possibility of generating microporous frameworks by removing the guest molecules has therefore been investigated. Hence, the stability of the different frameworks upon removal/reintroduction of the guest molecules has been monitored in detail, using elemental analysis, TGA and XRPD techniques.

In the TGA curves of all compounds,[70] the first weight loss in the temperature range 71-201 °C (see section 3.3), corresponds to the loss of the coordinated waters and guest water molecules. The loss of the coordinated aqua ligands is not observed below about 180 °C, apparently as the result of their strong coordination to the Zn(II) centers. Upon evacuation at 140 °C for 8 h under reduced pressure, five compounds **6-9** and **11,** which consist of acetate (**6**) and propionate (**7-9** and **11**) ligands experience weight losses consistent with the removal of all water molecules, behaving as second generation porous coordination polymers which have rigid vacant channels formed after the removal of guest molecules (Scheme 3.1). The results are as shown below in Table 3.6.

The weight loss of compound **1** consists of all water molecules and four formate groups when elevating the temperature to 140 °C for 8 h under vacuum. The X-ray powder diffraction reveals the remaining microcrystalline solid with a structure change (Figure 3.21A) according to the result of the elemental analysis and corresponds to the formula of Zn(**4,4'-bpy**)$_{2.5}$(ClO_4)$_2$, calcd.: C 45.86, H 3.07, N 10.70: found: C 44.67, H 3.01, N 10.56 (Table 3.6). This behavior is also observed in the remaining formate compounds **2-5.** Therefore, the zinc(II)-formate compounds containing **4,4'-bpy** organic ligand are unstable at high temperature, and this also happens with all metal-formate compounds in the present study (**1-5**). On the other hand after removal of the guest molecules from crystalline **7**, the XRPD pattern of the resulting material **7c** is almost identical to the theoretical one of the original material **7** (Figure 3.21D). These data clearly suggest that **7c** exhibits the original structure of **7** with empty channels. A similar behavior is also observed for compounds **6**, **8**, **9**, **11** (Figures 3.21C, E-G), therefore indicating that the solid-state structures of all compounds do not collapse when the water or water-formate molecules are taken out. Interestingly, the guest water species can be reintroduced into the evacuated samples of compounds **6-9** and **11** by simple immersion in water for 48 h, as confirmed by XRPD measurements (Figure 3.21), and elemental analyses (Table 3.6). In case of compound **1** the elemental analysis data after reintroduction of water indicates the formula to be Zn(**4,4'-bpy**)$_2$(H_2O)(ClO_4)$_2$, calcd.: C 40.39, H 3.05, N 9.42: found: C 41.43, H 3.50, N 8.96 (Table 3.6) and the XRPD is different from the original material indicating the change in structure, while the guest water molecules in

compounds **3-5** cannot be reintroduced after immersing in aqueous solution; the elemental analysis results confirm this feature (Table 3.6).

Scheme 3.1

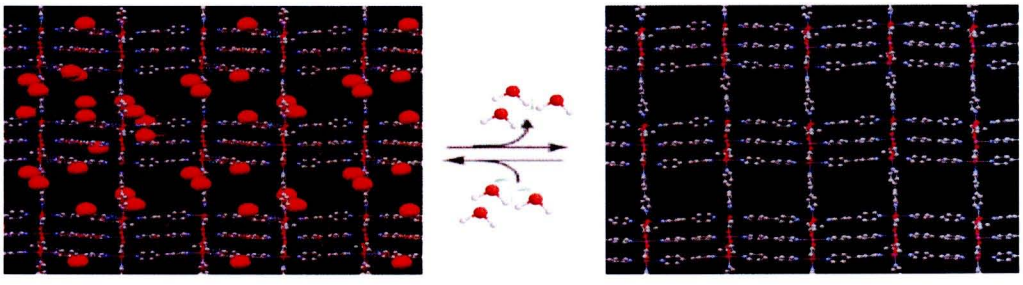

Table 3.6 Elemental analyses of compounds **1, 3-9** and **11** and of the products after removal and after reintroduction of the guest water molecules.

Compound	Element	Before Removal of water		After Removal of water		After water reintroduction
		Exp. (%)	Cal. (%)	Exp. (%)	Cal. (%)	Exp. (%)
1	C	39.22	39.23	44.67	41.76	41.43
	H	3.31	3.37	3.01	2.88	3.50
	N	8.22	8.21	10.56	8.74	8.96
3	C	39.53	40.09	44.56	42.72	43.72
	H	3.69	3.45	2.76	2.94	3.37
	N	9.56	8.39	10.36	8.94	10.09
4	C	31.09	30.68	40.11	34.67	39.96
	H	3.59	3.22	2.52	2.18	2.71
	N	6.04	5.96	8.75	6.74	8.33
5	C	45.61	44.51	48.31	48.51	47.76
	H	4.80	3.97	3.16	3.32	3.97
	N	12.83	11.98	13.8	13.50	12.89
6	C	36.41	36.40	38.68	38.33	37.04
	H	3.23	3.33	2.80	3.50	3.16
	N	6.30	6.70	7.81	7.06	7.09
7	C	51.19	50.97	53.19	53.23	49.30
	H	4.84	4.51	4.09	4.22	3.93
	N	9.91	9.91	10.36	10.35	9.51
8	C	41.43	42.34	44.19	44.51	42.43
	H	4.34	4.10	3.36	3.74	3.71
	N	7.51	7.60	7.20	7.99	7.75
9	C	41.16	40.81	46.96	45.06	41.93
	H	5.09	4.61	4.03	3.93	2.63
	N	8.12	7.43	9.19	8.08	9.36
11	C	47.09	47.06	50.18	50.48	47.29
	H	4.45	4.71	3.97	4.24	4.70
	N	10.59	10.55	11.02	11.32	11.06

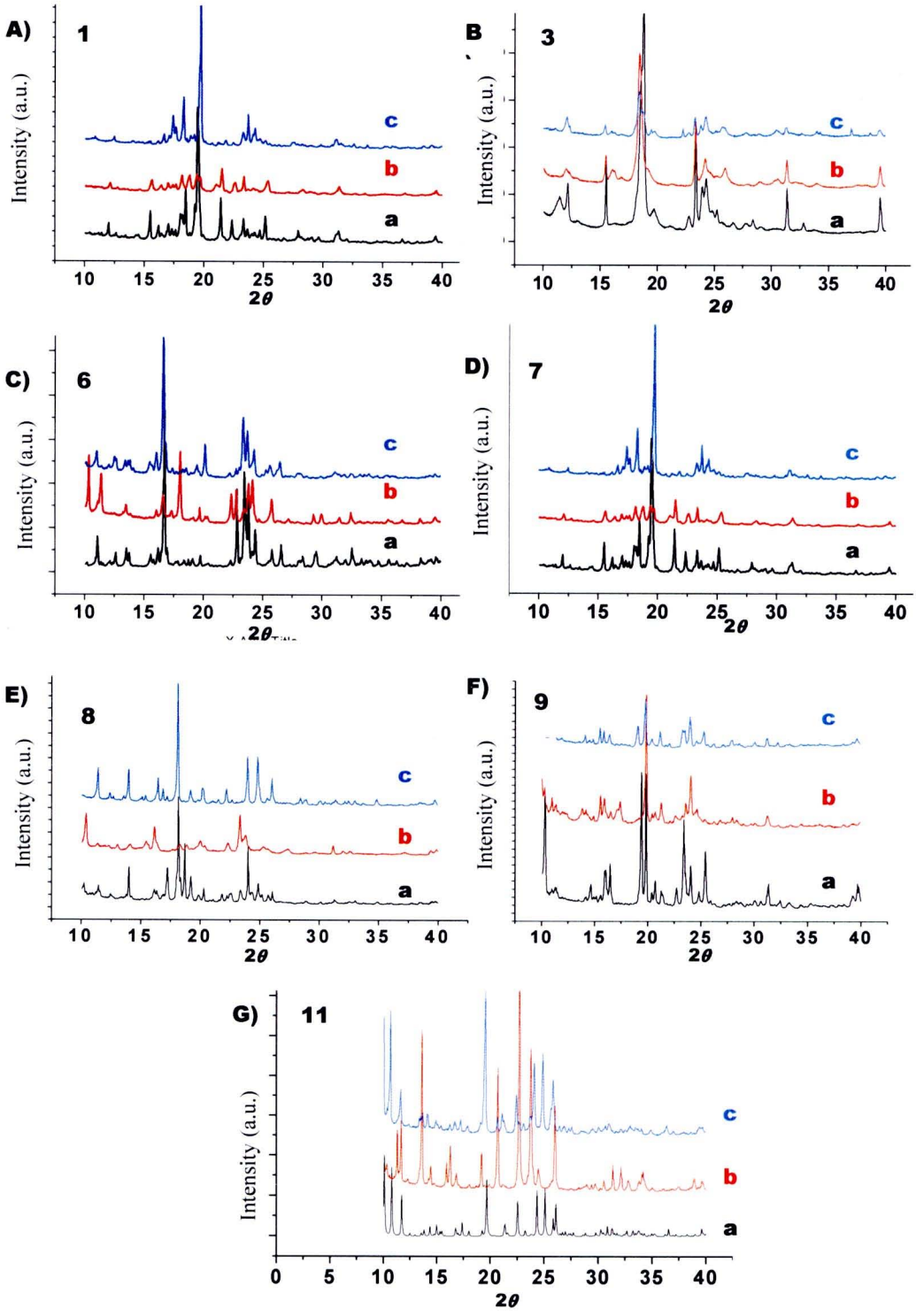

Figure 3.21 A)-G) XRPD patterns of **1**, **3**, **6-9** and **11**, respectively; (a) as-synthesized, (b) after removal of the guest water molecules, and (c) after reintroduction of the guest water molecules.

Thus, after removal of the water or water/formate molecules, the microporous solids $Zn(\mathbf{4,4'\text{-}bpy})_{2.5}(ClO_4)_2$ (**1c**), $\{Zn_3(\mathbf{4,4'\text{-}bpy})_3(\mu\text{-}O_2CCH_3)_4(PF_6)_2\}_n$ (**6c**), $\{Zn_3(\mathbf{4,4'\text{-}bpy})_4(\mu\text{-}O_2CCH_2CH_3)_4(ClO_4)_2(\mathbf{4,4'\text{-}bpy})_2\}_n$ (**7c**), $\{[Zn_3(\mathbf{4,4'\text{-}bpy})_4(\mu\text{-}OOCC_2H_5)_4](PF_6)_2\}_n$ (**8c**), $\{[Zn_2(\mathbf{4,4'\text{-}bpy})_2(\mu\text{-}OOCC_2H_5)_2(OH)](BF_4)\}_n$ (**9c**) and $\{[Zn_3(\mathbf{4,4'\text{-}bpy})_4\ (\mu\text{-}OOCC_2H_5)_4)_2](NO_3)_2\}_n$ (**11c**) are generated with retention of the original frameworks (for compounds **6-9** and **11**). Such microporous materials with high-thermal stabilities and host-guest properties are relatively rare and have therefore great potential for practical applications.

3.6 Counteranion Exchange Properties

3.6.1 Anion Exchange Procedure

The procedure of a typical counteranion exchange is outlined: An aqueous solution (10 mmol) containing a certain anion, ($KClO_4$, KPF_6, $NaBF_4$, or CF_3SO_3Na) was added to a suspension (1 mmol) of each microcrystalline sample in water (5 mL) at room temperature. The mixture was kept at room temperature for seven days before filtration. The solids collected by filtration were washed with several aliquots of water and ethanol before being characterized by infrared spectroscopy, elemental analyses and X-ray powder diffraction. The exchanged species are compared with those of the corresponding compounds prepared from the direct reaction. The exchanged species still give a sharp X-ray powder diffraction pattern.

3.6.2 Counteranion Exchange

The anion exchange properties of the nine porous coordination polymers, **1-4** and **6-10** have been investigated using X-ray powder diffraction (XRPD), elemental analysis and infrared (IR) spectroscopy. The experimental was performed by immersion of each compound in an aqueous solution containing different anions for seven days. The results are shown in Table 3.7. Compound **1** leads to complete replacement of ClO_4^- with only PF_6^-. The IR spectrum of **1** shows an intense ClO_4^- absorption band at 1089-1040 cm^{-1} (Figure 3.22a).[92] However, this absorption band disappears after the complete anion exchange. Instead, new and intense PF_6^- bands show up at 846-838 cm^{-1} (Figure 3.22c). Other peaks of the spectrum remain virtually unchanged, suggesting that the skeletal structure of the compound remains intact after

the exchange process with a high degree of crystallinity (Figure 3.23). This observation shows that the cavity of the exchanged compound is so flexible that PF_6^- anions may be incorporated instead of ClO_4^- anions, without structure collapse or decomposition. For example, the diffraction pattern closely resembles the experimental XRPD patterns of **1** (Figure 3.23A). IR spectrum and elemental analysis of the exchanged sample (Table 3.7) match that of $\{Zn_3(\mathbf{4,4'\text{-}bpy})_{3.5}(\mu\text{-}OOCH)_4(H_2O)_2(PF_6)_2(H_2O)_x\}_n$, **1**-$PF_6$ in which the quality of crystals is not good enough for

Table 3.7 Elemental analysis of Zn(II)/**4,4'-bpy**/carboxylate compounds and the products obtained from the anion exchange.

Compound	Element	Before exchange		After exchange (%)			
		Exp. (%)	Cal. (%)	ClO_4^-	PF_6^-	BF_4^-	$CF_3SO_3^-$
1	C	39.22	39.23		40.15		
	H	3.31	3.37	-	3.42	X	X
	N	8.22	8.21		9.41		
2	C	37.44	37.51	40.80			
	H	3.37	2.91	3.54	-	X	X
	N	8.01	7.85	8.76			
3	C	39.53	40.09	40.68	40.42		
	H	3.69	3.45	4.09	3.71	-	X
	N	9.56	8.39	10.14	9.60		
4	C	31.09	30.68	40.07	39.89		
	H	3.59	3.22	3.70	3.44	X	-
	N	6.04	5.96	9.92	9.46		
6	C	36.41	36.14	39.01			
	H	3.23	3.51	3.49	-	X	X
	N	6.30	6.70	7.77			
7	C	51.19	50.97		42.47		
	H	4.84	4.51	-	3.55	X	X
	N	9.91	9.91		8.15		
8	C	41.43	42.34	52.08			
	H	4.34	4.10	5.07	-	X	X
	N	7.51	7.60	10.03			
9	C	41.16	40.81	52.78	43.19		
	H	5.09	4.61	4.97	3.65	-	X
	N	8.12	7.43	9.79	8.09		
10	C	36.39	36.42	57.37	42.74	44.67	
	H	3.47	3.27	4.38	3.56	3.69	-
	N	6.92	6.07	13.47	9.05	10.28	

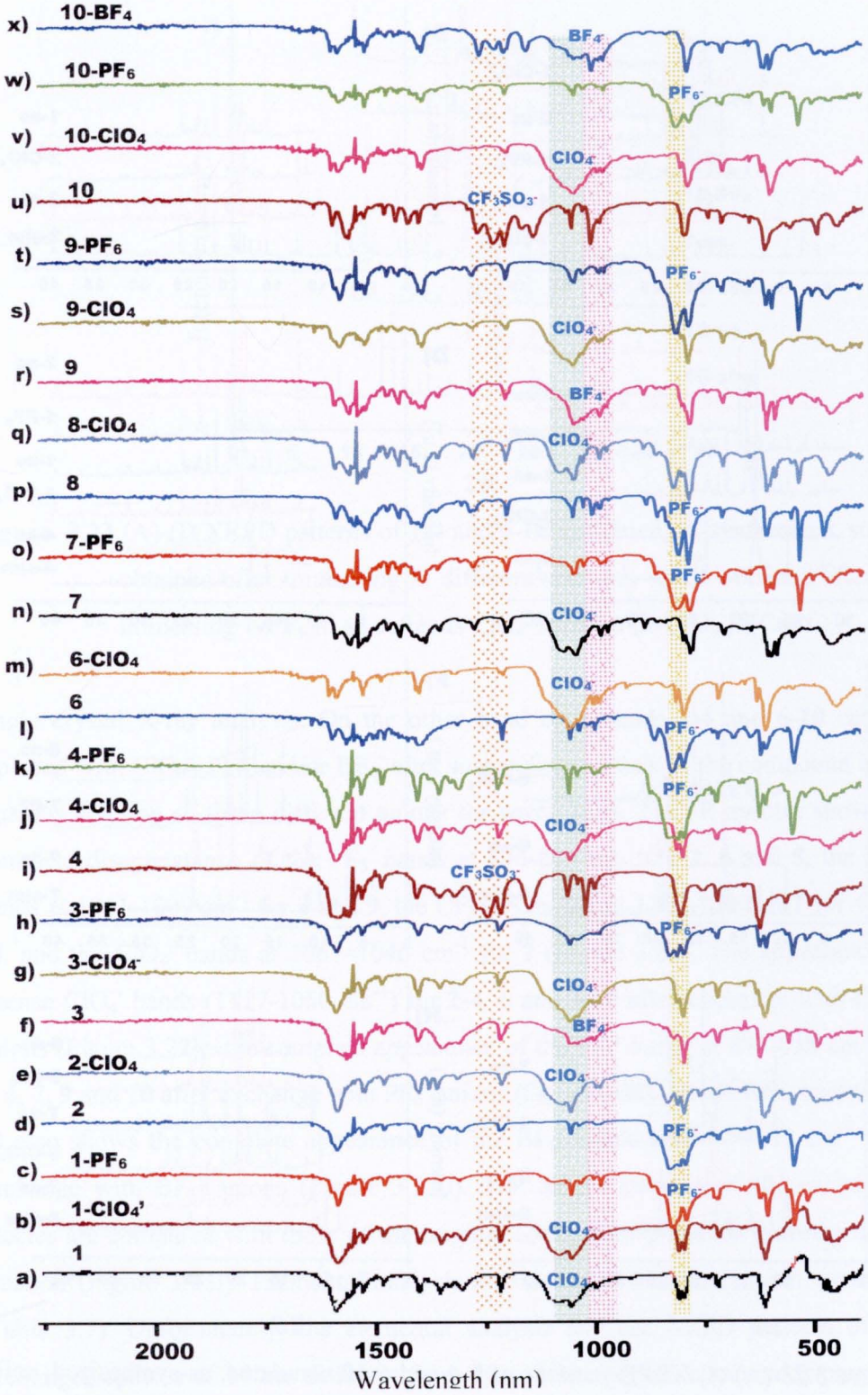

Figure 3.22 IR spectra of (a)-(w) **1-4** and **6-10** as-synthesized and after exchange with $KClO_4$ (**X**-ClO_4), KPF_6 (**X**-PF_6) and $NaBF_4$ (**X**-BF_4).

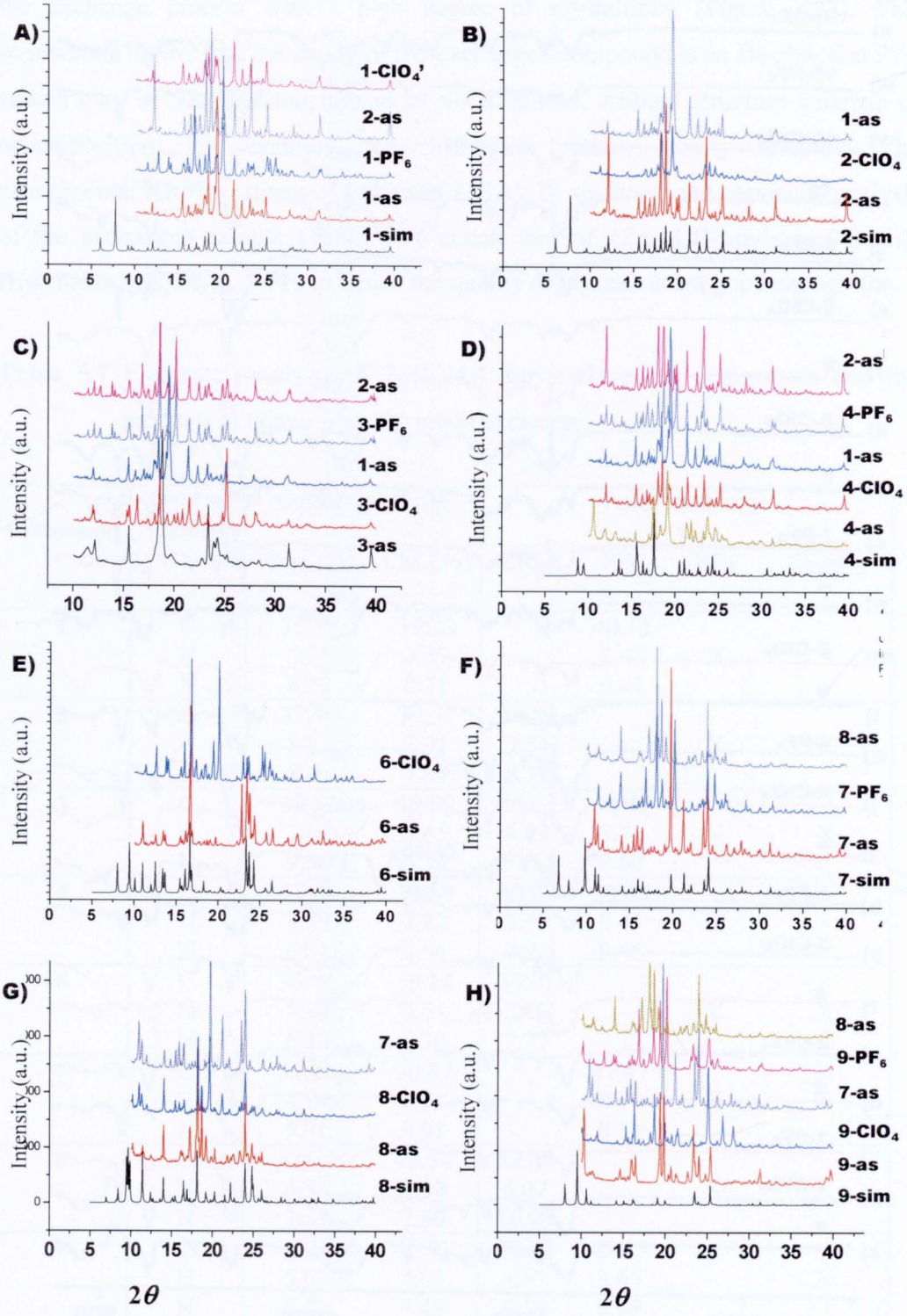

Figure 3.23 (A)-(I) XRPD patterns of **1-4** and **6-10** simulated, as-synthesized, solids obtained after immersing in different solution, solids obtained after re-immersing **1-PF$_6$** in an aqueous ClO_4^- solution (**1-ClO$_4$'**).

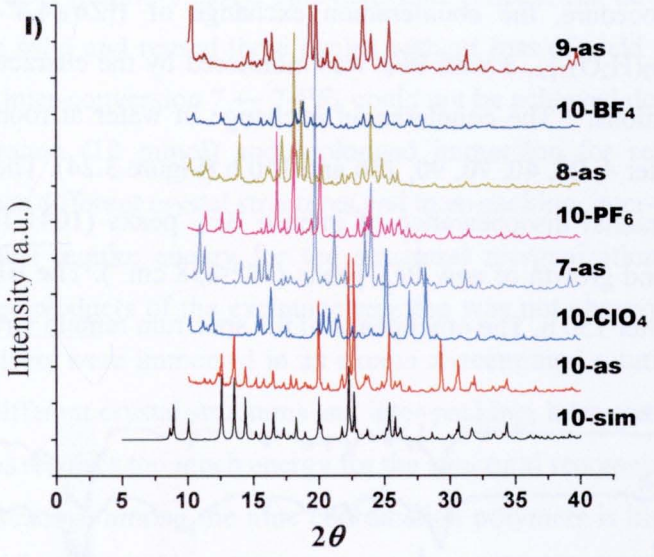

Figure 3.23 (A)-(I) XRPD patterns of **1-4** and **6-10** simulated, as-synthesized, solids obtained after immersing in different solution, solids obtained after re-immersing **1-PF$_6$** in an aqueous ClO_4^- solution (**1-ClO$_4$'**). **(Cont.)**

.

single crystal X-ray analysis. On the other hand compounds **2-4** and **6-10** can be replaced with ClO_4^-, PF_6^- and/or BF_4^- after suspending crystals of the compound in an aqueous solution of these different anions for seven days. The IR spectra show the complete disappearance of the PF_6^- bands at 846-820 cm^{-1} for **2**, **6** and **8**, the BF_4^- bands at 1041-1009 cm^{-1} for **3** and **9**, the $CF_3SO_3^-$ bands at 1257-1200 cm^{-1} for **4** and **10**, and the ClO_4^- bands at 1067–1046 cm^{-1} for **7** (Figure 3.22). The appearance of intense ClO_4^- bands (1117-1050 cm^{-1}) for **2-4**, **6** and **8-10** after exchange with ClO_4^- anions (Figure 3.22), the complete appearance of the PF_6^- bands at 841-838 cm^{-1} for **3**, **4**, **7**, **9** and **10** after exchange with PF_6^- anions (Figure 3.22). In addition, compound **10** also shows the complete appearance of the BF_4^- bands at 1041-1012 cm^{-1} after exchange with BF_4^- anions (Figure 3.22u). The XRPD patterns of the exchanged species are compared with those of the original compounds prepared from the direct reaction (Figure 3.23I). Elemental analysis also supports complete anion exchange (Table 3.7). Unfortunately, the elemental analysis and the XRPD patterns of the exchanged species of **10** are different from that of the original compounds prepared from the direct reaction (Figure 3.23I and Table 3.7). This means that the products must have been transformed to new crystal packing structures. To investigate the

exchange procedure, the counteranion exchange of $\{[Zn_3(\mathbf{4,4'\text{-}bpy})_{3.5}(\mu\text{-}OOCH)_4(H_2O)_2](BF_4)_2(H_2O)_2\}_n$, **3** with PF_6^- was monitored by the characteristic IR bands of the counteranions.[51] The counteranion exchange in water at room temperature was monitored after 4, 20, 40, 70, 90, 130 and 150 h (Figure 3.24). The infrared spectrum shows the gradual disappearance of intense BF_4^- peaks (1041-1009 cm^{-1}) and the appearance and growth of new PF_6^- peaks (842-838 cm^{-1}). The BF_4^- peaks disappear completely after 150 h. The other peaks of the spectrum remain virtually unchanged.

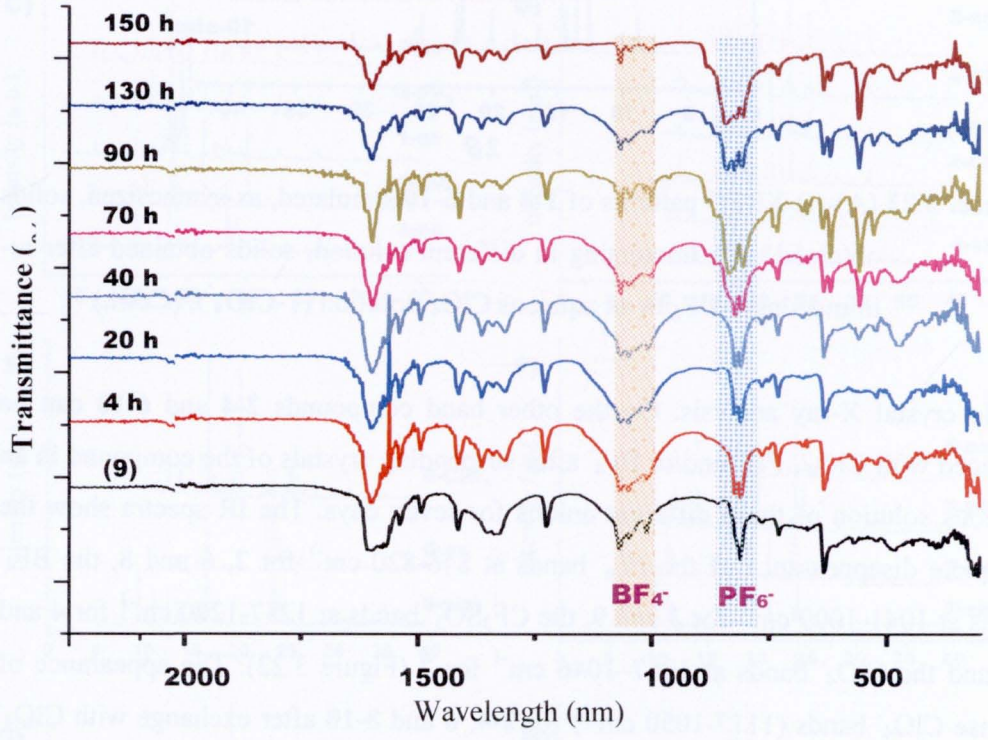

Figure 3.24 IR spectra change procedure during the counteranion exchange of **3** with KPF_6 in function of the time on the solid, dried samples.

The reverse processes of products, **1**-PF_6 and **7**-PF_6 which were prepared by anion exchange have been investigated. The ClO_4^- anions of the original compounds **1** and **7** were replaced by the slightly larger PF_6^- anions, giving the product **1**-PF_6 and **7**-PF_6 (Figures 3.23A and F). Both **1**-PF_6 and **7**-PF_6 were re-immersed in an excess aqueous ClO_4^- solution. Surprisingly, only **1** was observed the reversible process and the quality of the so-obtained **1-ClO_4'** is similar as the original one for **1,** even when crystals of **1-PF_6** were re-immersed in an excess concentrated solution (10 mmol) of

$NaClO_4$ for seven days (Figure 3.23A). This reversible process can be easily studied by filtration of the solid and reused three cycles without loss of yield or selectivity. Contradictory, the inter-conversion **7** ↔ **7-PF$_6$** could not be achieved despite the used high salt concentration (10 mmol) and prolonged immersion for seven days. Its product probably has different crystal structures and inter-packing, inter-conversion of the compounds must require energy for the structural reorganization. The reverse process of the other products of the exchange reaction was not observed even when crystals of all products were immersed in an excess concentrated solution. Since the compounds have different crystal structures and inter-packing, inter-conversion of the compounds perhaps requires too much energy for the structural reorganization.

The anion exchange among the nine coordination polymers is highly selective and the anions in the original compounds can be totally replaced with PF_6^- for **1, 3**, **4**, **7**, **9** and **10**, ClO_4^- for **2-4**, **6** and **8-10**, and BF_4^- for **10**. Selectivity of anion exchange has been observed in several coordination polymers,[77,78] but its mechanism is not well understood. In some cases, anion exchange is accompanied by bond formation or dissociation[77] and a recent study showed that the irreversibility of the exchange of $Ag(bpp)ClO_4$[93] (bpp = 1,3-bis(4-pyridyl)propane) with PF_6^- is attributed to the formation of Ag–Ag interactions in $Ag(bpp)PF_6$ and the exchanges of $AgLClO_4$[78] (L = *N,N'*-bis-(3-pyridine-carboxamide)-1,6-hexane) with NO_3^- and $CF_3SO_3^-$ are not reversible, because of different crystal structures and inner-packing. Anion selectivity could be due to the different hydration energy, guest anion volume of the anions and the structural reorganization involved in the conversion. Thus, it is likely to be the reason for the selective exchange observed in the present compounds. Selectivity of anion exchange has been widely observed in anion resins and was shown to be governed by the hydration energy (ΔG_h) and the guest anion volume, which is a function of its radius and charge.

The exchange of **1, 3**, **4**, **7**, **9** and **10** with PF_6^- is favored, as the guest anion volume of ClO_4^- (52.1 cm^3 mol^{-1}) is just smaller than that of PF_6^- (56.2 cm^3 mol^{-1}). The exchange of these compounds with BF_4^- (guest anion volume = 51.0 cm^3 mol^{-1}) cannot be observed with compounds **1**, **3**, **4**, **7** and **9,** due to the pronounced effect of different hydration energy. So far only the exchange of compound **10** has been achieved, which could be due to the dominance of the guest anion volume. Although

the guest anion volume of $CF_3SO_3^-$ ion is not known, it is expected to be much bigger than those of ClO_4^-, PF_6^- and BF_4^-. The difference in guest anion volume between ClO_4^-, PF_6^- and BF_4^- and the others $CF_3SO_3^-$ may explain the fact that the exchanges of all compounds with $CF_3SO_3^-$ are not feasible.

For a better understanding, however, all exchanged products anions should be investigated by single crystal X-ray structures. In some cases, considerable structural reorganization would be involved in such an exchange, which may render the process unfavorable.

3.7 Catalytic Properties

3.7.1 Catalytic Reactions

Reduction in negative environmental impact, which in the past was often caused by some chemical industries, presents nowadays a major scientific challenge. One possible search for a cleaner chemical process is new selective catalysts, because improved catalysts can decrease the number of stages in a given process and hence diminish its impact on the environment. In terms of a so-called "green chemistry approach", it seems still more important to design catalysts that can be reused and recycled easily. In this sense, it is very understandable that there currently is considerable interest in metal organic polymeric materials inspired by their intriguing structural diversity and potential functions, such as microporous solids for molecular adsorptions, ion exchange, and heterogeneous catalysis.[1-10] In this sense, it is worth mentioning Fujita's work[93] on coordination polymers applications. From the reported studies, **4,4'-bpy** ligand is well known and has been found to be useful as a building block in construction of organic-inorganic materials with desired topologies. Particularly, previous studies on the a square network $\{Cd(\mathbf{4,4'\text{-}bpy})_2(H_2O)_2(NO_3)_2{\cdot}4H_2O\}_n$,[93] have proven to possess interesting catalytic properties in cyanosilylation of aldehydes and imines reactions (Scheme 3.2). On the other hand, some additional ligands can modify structure and properties of the resulting compounds, and it is clear that the catalytic activity of the so-called MOF would strongly depend on the nature of both the organic linker and metal ion as well as additional ligands present in the structure. Monocarboxylate ligands have proved to be

extremely important ligands for metals, and the obtained metal compounds often show attractive chemical and physical properties.

Scheme 3.2

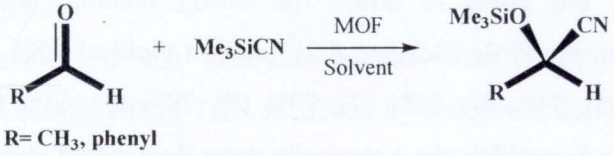

R= CH_3, phenyl

3.7.2 Cyanosilylation Reaction

A typical cyanosilylation reaction was performed as follows: 40 mg (0.006 mmol, 0.2 mmol of Zn(II)) of the MOF catalyst was suspended in 5 mL of dry dichloromethane (CH_2Cl_2) or tetrahydrofuran (THF), followed by the addition of the aldehyde (1.5 mmol) and trimethylsilyl cyanide (3 mmol). The reaction mixtures were stirred at room temperature under argon for 24 h. The reaction conversions were determined by gas chromatography (GC) analysis. The catalytic recyclability was checked three times with the same batch of catalyst, and no obvious decrease in activity was observed. The heterogeneity of the catalyst reaction was investigated by filtration test. The catalyst was separated after a reaction time of 5 h and the solution was divided into two equal portions. Hereafter, one portion was stirred with fresh catalyst, while the second one was stirred without the MOF catalyst.

3.7.3 Catalytic Reactivity

Porous MOFs **1-11** have been tested as heterogeneous catalysts for the cyanosilylation of acetaldehyde and benzaldehyde. Thus, the selectivity and activity of the three-dimensional framework (**1-3**), the two-dimensional layered networks (**4, 5, 7** and **9**), and the one-dimensional triple-stranded ladders (**6**), zig-zag double-stranded ladders (**8** and **11**) and double-stranded ladders (**10**) have been examined (Figure 3.17).

Blank reactions have been performed by carrying the cyanosilylation of acetaldehyde and benzaldehyde without catalyst, at 25 °C. These test reactions give only conversions of 18% for acetaldehyde and 10% for benzaldehyde, after a reaction time of 24 h. When 40 mg of solid **1** is used as catalyst, a conversion of 95% of

acetaldehyde is reached after 24 h reaction time in CH_2Cl_2 (Table 3.8 and Figure 3.25). This high conversion suggests first of all that **1** acts as a very efficient catalyst for this reaction, and that both acetaldehyde and trimethylsilyl cyanide can diffuse swiftly through the pores to attain the Lewis metallic sites, to generate 2-(methylsiloxy)-propionitrile (Scheme 3.2)[55] with a yield of 95% (90% (**2**), 94% (**3**), 91% (**4**), 84% (**5**), 71% (**6**), 86% (**7**), 70% (**8**), 79% (**9**), 53% (**10**) and 76% (**11**), Table 3.8). When benzaldehyde, a sterically more demanding substrate, is used under similar reaction conditions, a conversion of only 22% is observed (16% (**2**), 13% (**3**), 26% (**4**), 18% (**5**), 21% (**6**), 22% (**7**), 14% (**8**), 4% (**9**), 17% (**10**) and 13% (**11**), Table 3.8). This significantly lower reactivity suggests that the dimension of the channels of the MOF plays an important role and leads to size selectivity.

Next, the influence of another organic solvent, namely THF, on the conversion of acetaldehyde has been examined for each MOF catalyst. It has been found that the reaction is less efficient in THF, which may be explained by a competitive binding of the substrate and the donor type solvent to the metal site. This competitive binding obviously does not occur with CH_2Cl_2. For instance, in THF, compound **1** promotes the conversion of only 38% acetaldehyde (26% (**2**), 56% (**3**), 31% (**4**), 56% (**5**), 30% (**6**), 57% (**7**), 67% (**8**), 61% (**9**), 39% (**10**) and 60% (**11**), Table 3.8).

It is noted that the catalytic reactivities of compounds **8** and **11** in THF are higher than other compounds. This might be due to the smaller number of donating water ligand/asymmetric unit. As a result, the zinc(II) centers of **8** and **11** are more cationic than other compounds, the Lewis acidity increases leading to the more effective binding of the substrate and giving high conversion (67% for **8** and 60% for **11**) for THF. The cationic nature and Lewis acidity of the Zn^{2+} center may play a role and lead to significantly different in the conversion.

The catalytic activities of compounds **1-11** for the cyanosilylation of aldehydes have been compared with those of other porous coordination frameworks. Fujita and co-workers reported the first two-dimensional coordination polymeric catalyst, *i.e.* $\{Cd(\mathbf{4,4'\text{-}bpy})_2(NO_3)_2\}_n$,[41] for the cyanosilylation of aldehydes. This square network material is highly shape-selective, which is illustrated by the inclusion of *ortho*-dihalogenobenzenes, whereas the *meta*- and *para*-isomers do not form clathrates. Shape specificity has been observed as well with this compound for the

aldehydes and ketones, as well as the Mukaiyama-aldol reaction. In each case, a pronounced size-selectivity effect consistent with the pore dimensions is observed.

3.7.4 Heterogeneity

The heterogeneity of the catalytic reaction has been probed for the cyanosilylation of acetaldehyde in THF, mediated by compound **1**. Thus, the catalyst (compound **1**) has been filtered out after a reaction time of 5 h, corresponding to an acetaldehyde conversion of 24% (Figure 3.26). The filtrate has been stirred for 24 h and no further conversion of the substrate is observed (about 25% conversion; Figure 3.26). This result clearly demonstrates that no homogeneous catalytic species is present in solution. Next, the filtrate has been divided into two equal parts. The first part has been stirred with fresh catalyst **1,** while the other one has been stirred without catalyst. In the filtrate without catalyst, the reaction does not proceed further, whereas in the catalyst-containing suspension, the conversion of the substrate is observed, reaching 38% after 24 h (Figure 3.26). Thus, the catalytic activity of Zn(II)-**4,4'-bpy**-carboxylato originates from the presence of the solid catalyst and is not due to molecular species that dissolve into the solution. Furthermore, the isolated catalyst (by filtration after a reaction time of 24 h) can be reused without apparent loss of activity.

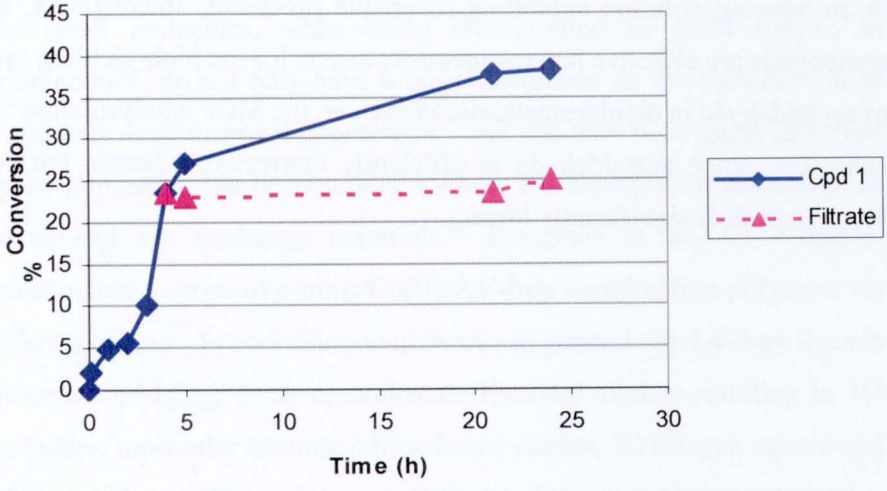

Figure 3.26 Cyanosilylation of acetaldehyde in THF catalyzed by **1** and the effect of filtration.

3.8 Conclusions

In present chapter, the influence of small secondary ligands, namely formato, acetate and propionato ligands, on the overall solid-state structure of zinc(II)–**4,4-bpy**–carboxylato coordination polymers has been investigated. This study shows that the change from a formato ligand to an acetato and a propionato ligand gives rise to the formation of drastically distinct metal-organic frameworks, as the result of the different steric bulk of the carboxylato unit involved. Such studies are of great interest for the crystal engineering chemist and this field is expected to contribute to an increase of knowledge about crystallization processes and framework design and structure prediction.

The work presented in this chapter also describes the thermal and optical properties, potential cation-exchange properties with structure retention by doping zinc(II) compounds with copper(II) and manganese(II), anion-exchange and catalytic reactivity, as well as dynamic structural transformation by removal and reintroduction of guest molecules for eleven novel coordination polymers, belonging to the second generation of porous coordination compounds. The removal/reintroduction of water guest molecules is accompanied by a crystalline-to-crystalline structural transformation for five porous materials (**6-9** and **11**), which exhibits rigid vacant host channels. Furthermore, compound **1** shows quite interesting anion-sensing properties in an aqueous solution exhibiting reversible processes. Interestingly, these zinc(II) compounds are effective heterogeneous catalysts for the high-yielding cyanosilylation of acetaldehyde in dichloromethane. Moreover, the MOF catalysts show size-selective behaviors, since acetaldehyde is efficiently converted, whereas the conversion of benzaldehyde is significantly lower.